Controls on Global Mantle Convective Structures and Their Comparison With Seismic Models

Wei Mao[1] (ID) **and Shijie Zhong[1]** (ID)

[1]Department of Physics, University of Colorado Boulder, Boulder, CO, USA

Abstract Seismic observations suggest (1) significant accumulation of subducted slabs above the 670-km discontinuity in many subduction zones, (2) possible structure change at ~1,000-km depth, and (3) the large low shear wave velocity provinces above the core-mantle boundary in the African and Pacific lower mantle be associated with chemical heterogeneity. Global mantle convection models with realistic plate motion history reproduce most of these structures. However, it remains unclear how the convection models compare with seismic models at different spatial wavelengths and depths. By conducting quantitative analysis between mantle convection and seismic models, we found that mantle convective structures show significant correlations with seismic structures in the upper mantle and mantle transition zone for wavelengths up to spherical harmonic degree 20. However, the global correlation is weak at intermediate to short wavelengths (for degrees 4 and higher) in the lower mantle below ~1,000-km depth. A weak layer beneath the spinel-to-postspinel phase change help consistently reproduce stagnant slabs in the western Pacific, while having insignificant effects elsewhere, that is, the large low shear wave velocity province structures. The cold slab structures and their correlations with the seismically fast anomalies are nearly identical for our convection models with and without the plumes, indicating that seismically fast anomalies in the mantle mainly result from the subducted slabs. Models with viscosity increase at 1,000-km depth and the 670-km depth phase change may reproduce seismic slab structures including the stagnant slabs in the mantle transition zone equally well as models with a thin weak layer below the 670-km phase boundary.

1. Introduction

Studies of mantle seismic structure have significantly improved our understanding of the structure and dynamics of the Earth's mantle since the landmark paper published about 40 years ago (Dziewonski et al., 1977). Global seismic models consistently show that the circum-Pacific seismically fast velocity anomalies separate the African and Pacific seismically slow velocity anomalies (i.e., large low shear wave velocity provinces (LLSVPs)) from 1,000-km depth to the core-mantle boundary (CMB), giving rise to the so-called degree-2 mantle structure (Dziewonski et al., 1977; French & Romanowicz, 2014, 2015; Houser et al., 2008; Masters et al., 2000; Panning & Romanowicz, 2006; Ritsema et al., 2011, 1999; Su et al., 1994; Tanimoto, 1990). Regional and global seismic tomographic models of subduction zones show that some subducted slabs extend continuously from the upper mantle to the CMB (e.g., Grand et al., 1997; van der Hilst et al., 1997). These seismic studies demonstrate that significant mass flux occurs across the 670-km discontinuity (i.e., the upper and lower mantle boundary), thus supporting the whole mantle convection model (e.g., Grand et al., 1997) over the layered mantle model that had been favored by some geochemical arguments at the time (e.g., Hofmann, 1997). The whole mantle model is further supported by the success of mantle flow models of the long-wavelength geoid that use the seismic structure as a proxy of mantle buoyancy (Hager et al., 1985; Ricard et al., 1993).

However, two important features in seismic structures that have emerged from recent seismic studies may not be in agreement with simple whole mantle convection model. The first is the African and Pacific LLSVPs that may display different chemical composition from the rest of the mantle (e.g., He & Wen, 2012; Ishii & Tromp, 1999; Masters et al., 2000; Ni et al., 2002; Su & Dziewonski, 1997; Wen et al., 2001). The second is that subducted slabs show distinctly different morphologies around the 670-km discontinuity (e.g., Goes et al., 2017). While at some subduction zones (for example, North America and the Central America), slabs penetrate into the lower mantle and reach the CMB (e.g., Grand et al., 1997; van der Hilst et al., 1997), at other subduction zones, slabs appear to be deflected,

flattened, and stagnant above the 670-km depth (e.g., in Honshu, Bonin, and Chile (French & Romanowicz, 2014; Fukao et al., 2001; Fukao et al., 2009; Fukao & Obayashi, 2013; Ritsema et al., 2011)) or around the 1,000-km depth (e.g., in Tonga, Kermadec, and Java subduction zones (Fukao & Obayashi, 2013)). However, slab stagnation at ~1,000-km depth is not a consistent feature among seismic tomographic models, as pointed out in Goes et al. (2017) and Mao and Zhong (2018). At ~1,000-km depth apparent change in mantle upwelling structure was also proposed (e.g., French & Romanowicz, 2015). Rudolph et al. (2015) suggested that an increase of mantle viscosity at ~1,000-km depth, which they inferred from inverting the geoid, may be responsible for these seismic structures around 670–1,000-km depths.

A large number of geodynamic studies have been done to understand the origin and dynamics of the African and Pacific LLSVPs and slab structures. McNamara and Zhong (2005) showed that the morphology and structure of the African and Pacific LLSVPs are well explained in global mantle convection models that treat the anomalies as thermochemical (hot and intrinsically dense) features and include plate motion history for the last 120 Myr (million years), consistent with other studies (e.g., Bower et al., 2013; Davaille, 1999; Steinberger et al., 2012; Zhang et al., 2010; Zhong & Rudolph, 2015). However, it is still debatable whether chemical anomalies are required in mantle convection models to explain the LLSVP (Davies et al., 2012; Zhong & Liu, 2016). Regional and global convection models with plate motion and subduction history for the last 100–120 Myr have been formulated to interpret the long linear seismic structure of the Farallon and Tethys slabs in the lower mantle (e.g., Bunge & Grand, 2000; Lithgow-Bertelloni & Richards, 1998; Liu et al., 2008; Ricard et al., 1993). Slab structures in the upper mantle may depend on trench motion and slab rheology as suggested in generic mantle dynamic models (e.g., Agrusta et al., 2017; Billen & Hirth, 2007; Christensen, 1996; Garel et al., 2014; Goes et al., 2017; Holt et al., 2015; Lee & King, 2011; Stegman et al., 2006; Yang et al., 2018; Zhong & Gurnis, 1995). Recently, Mao and Zhong (2018) (referred to as MZ18 hereafter) showed that the primary characteristics of slab structures including the stagnant slabs in the western Pacific mantle transition zone and linear slab structures in the lower mantle beneath Americas and Asia can be explained in a global convection model that incorporates thermally insulating CMB condition, the spinel-to-postspinel phase change at the 670-km depth and a weak layer below the phase boundary and is otherwise similar to that in studies of the LLSVP (e.g., McNamara & Zhong, 2005).

In spite of the apparent success of these global convection models in explaining the seismic structures including the LLSVP and slabs (e.g., Mao & Zhong, 2018; McNamara & Zhong, 2005), three important points need to be addressed. First, no attempt has been made to compare quantitatively these new convection models with seismic models and with mantle dynamic models previously constructed under different model assumptions (e.g., Ricard et al., 1993; Lithgow-Bertelloni & Richards, 1998; Steinberger, 2000, Steinberger et al., 2012). Second, because the convection model for slabs by MZ18 used a thermally insulating boundary condition at the CMB to restrict formation of large-scale upwelling plume structures at the CMB including the LLSVP, it is important to test to what extent a more realistic isothermal CMB would affect slab structures or a weak layer below the spinel-to-postspinel phase boundary in MZ18 would affect the LLSVP structures. Third, how the proposed increase of mantle viscosity at ~1,000-km depth (Rudolph et al., 2015) affects mantle convective structures (e.g., the slabs) and how well the resulting mantle convective structures correlate with seismic models are not fully examined. The main objective of this study is to answer these three questions. It should be noted that a number of previous studies have quantitatively compared lower mantle convective structures with that in seismic models (e.g., Bull et al., 2009; Schuberth et al., 2009; Shephard et al., 2012). In particular, Becker and Boschi (2002) compared different seismic tomographic models (e.g., Ritsema et al., 1999) with mantle dynamic models (Lithgow-Bertelloni & Richards, 1998; Steinberger, 2000) by quantifying the correlation among different models for the whole mantle. Our correlation analyses largely follow Becker and Boschi (2002).

This paper is organized as follows. In the next section, we will describe the mantle convection models including the imposed surface plate motion history, spinel-to-postspinel phase change, mantle viscosity, and compositional heterogeneities. We will then present different mantle convection model results and compare them with seismic tomographic and previous convection models by quantifying correlations at different depths and horizontal length scales. The discussions and conclusions will be presented in the final two sections.

2. Methods and Model Setup

Our global convection models may consider depth- and temperature-dependent viscosity, depth-dependent thermal expansivity and thermal diffusivity, spinel-to-postspinel phase change, plate motion history as surface boundary conditions, and chemically dense materials above the CMB. The models are similar to that in McNamara and Zhong (2005) and MZ18.

2.1. Governing Equations for Thermal Convection With Phase Changes

Our models of mantle convection are formulated in the three-dimensional spherical shell geometry with the Boussinesq approximation and infinitely large Prandtl number. The models may include mantle phase changes and depth- and temperature-dependent viscosity. The governing equations are the conservation equations of the mass, momentum, and energy, and the nondimensional equations are the following (Christensen & Yuen, 1985; McNamara & Zhong, 2004; Zhong et al., 2000, 2008):

$$\nabla \cdot \overrightarrow{u} = 0, \tag{1}$$

$$-\nabla P + \nabla \cdot (\eta \dot{\varepsilon}) + \left[Ra(T - BC) - \sum_j Rb^j \Gamma_j \right] \hat{e}_r = 0, \tag{2}$$

$$\frac{\partial T}{\partial t} + (\overrightarrow{u} \cdot \nabla) T = \nabla^2 T + H, \tag{3}$$

$$\frac{\partial C}{\partial t} + (\overrightarrow{u} \cdot \nabla) C = 0, \tag{4}$$

where $\overrightarrow{u}$ is the velocity vector; P is the dynamic pressure; η is the viscosity; $\dot{\varepsilon}$ is the strain rate tensor; T is the temperature; C is the composition field, which can be either 0 or 1 that represents the mantle and the chemically distinct and dense materials (i.e., that would form the thermochemical piles), respectively; Γ_j is a phase change function for the jth phase change if multiple change changes exist in the model; Ra and Rb^j are the thermal Rayleigh number and phase change Rayleigh number, respectively; B is the buoyancy ratio; $\hat{e}_r$ is the unit vector in radial direction; t is the time; and H is the internal heating generation rate.

Ra and Rb^j are defined as

$$Ra = \frac{\rho g \alpha \Delta T R^3}{\kappa \eta_0}, \tag{5}$$

$$Rb^j = \frac{\Delta \rho_j g R^3}{\kappa \eta_0}, \tag{6}$$

where ρ is the mantle reference density, g is the gravitational acceleration, α is the thermal expansivity, ΔT is the temperature difference between the surface and CMB, κ is the thermal diffusivity, η_0 is the reference viscosity, $\Delta \rho_j$ is the density jump for the jth phase change, and R is the radius of the Earth.

The heat production rate H is defined as

$$H = \frac{QR^2}{C_p \kappa \Delta T}, \tag{7}$$

where Q is the internal heat generation rate and C_p is the specific heat. In this study, we fix H to be 100 that leads to about 70–80% internal heating ratio in our models with isothermal CMB boundary condition. Such ratios are consistent with previous estimates based on plume excess temperature and heat flux observations (Leng & Zhong, 2008; Zhong, 2006).

B is the buoyancy ratio, which is the ratio of chemical to thermal density contrast and defined as

$$B = \frac{\Delta \rho_c}{\alpha \rho \Delta T}, \tag{8}$$

where $\Delta \rho_c$ is the density contrast between the two chemical components (i.e., chemical pile versus the normal mantle). In this study, B is 0.2 or 0.25 and the corresponding density differences are 49.5 and 61.9 kg/m³,

Table 1
Model Parameters

Parameters	Value
Earth's radius, R	6370 km
Mantle thickness, h	2870 km
Mantle density, ρ	3300 kg/m^3
Gravitational acceleration, g	9.8 m/s^2
Thermal expansivity, α[a]	3×10^{-5}/K
Reference temperature difference, ΔT	2500 K
Thermal diffusivity, κ[a]	10^{-6} m^2/s
Gas constant, R_{gas}	8.314 J/(K mol)
Specific heat, C_P	1250 J/(kg K)
Spinel to postspinel density change, $\Delta\rho_1/\rho$	8%
Spinel to postspinel phase change width, δ_1	40 km
Spinel to postspinel phase change reference depth, d_1	670 km
Spinel to postspinel phase change reference temperature, T_1	1573 K

[a]Thermal expansivity decreases by a factor of 2.5 from surface to the CMB, while thermal diffusivity increases by a factor of 2.18 from surface to the CMB.

Table 2
Input Parameters for Different Models[a]

Case	Time (Myr)	Depth (km)	β	γ (MPa/K)	Ra	SP	Botm	B
1	130	670	100	−2.0	5e7	1000	0	no
2	130	670	100	0	5e7	1	0	no
3	130	670	100	−2.0	5e7	1	0	no
4	130	670	100	−3.5	5e7	1	0	no
5	130	670	100	0	5e7	1000	0	no
6	65	670	100	−2.0	5e7	1000	0	no
7	200	670	100	−2.0	5e7	1000	0	no
8	130	670	100	−2.0	5e7	1000	1	0.2
9	200	670	100	−2.0	5e7	1000	1	0.2
10	458	670	100	−2.0	5e7	1000	1	0.25
11	130	670	100	−2.0	5e7	1000	1	no
12	200	670	100	−2.0	5e7	1000	1	no
13	458	670	100	−2.0	5e7	1000	1	no
14	200	670	100	−2.0	2e7	1000	1	no
15	200	670	100	−2.0	1e8	1000	1	no
16	458	670	100	−2.0	2e7	1000	1	no
17	130	1000	100	0	5e7	1	0	no
18	130	1000	100	−2.0	5e7	1	0	no
19	200	1000	100	−2.0	5e7	1	1	0.2
20	130	1000	100	−2.0	5e7	1	1	no
21[b]	130	670	100	−2.0	5e7	1000	0	no
22[b]	200	670	100	−2.0	5e7	1000	0	no

[a]*Time*, *Depth*, β, γ, *Ra*, *SP*, *Botm*, and *B* represent model total running time (in Myr), viscosity jump boundary at 670- or 1,000-km depth, viscosity increase at 670- or 1,000-km depth, Clapeyron slope (in MPa/K), Rayleigh number, and properties of the weak layer below the phase boundary, bottom thermal boundary condition (0 for insulating and 1 for isothermal boundary condition), and buoyancy number, respectively. The value for SP reduction represents the factor of viscosity reduction for the weak layer. When it is 1, no weak layer is present. [b]Cases 21 and 22 use plate motion model by Müller et al. (2016) instead of Seton et al. (2012).

respectively. Composition C and buoyancy ratio B are only relevant for thermochemical convection cases. The initial thickness of the chemical layer that is flat everywhere above CMB is 250 km, which leads to the volume of the intrinsically dense material to be comparable with seismic observations (e.g., He & Wen, 2012; Houser et al., 2008).

2.2. Mantle Phase Change and Viscosity Formulations

A phase change function formulation is used here to represent phase changes, and the formulation is the same as in Christensen and Yuen (1985) and Zhong and Gurnis (1994). The phase change function Γ_j is defined in dimensionless form as

$$\Gamma_j = \frac{1}{2}\left[1 + \tanh\left(\frac{\pi_j}{\delta}\right)\right], \tag{9}$$

where δ is the phase change width that measures the depth segment of phase change and π_j is the dimensionless "excess pressure" as

$$\pi_j = d - d_j - \gamma_j(T - T_j), \tag{10}$$

where d is the depth, d_j and T_j are the reference depth and temperature of phase change j, and γ_j is the Clapeyron slope. The Clapeyron slope is normalized by $\rho g R/\Delta T$.

In this study, we only consider the phase change at 670-km depth from spinel to postspinel phases for which phase change parameters are well known (Table 1). When Γ is smaller than 0.5, the spinel phase viscosity is applied even if it is below 670-km depth. When Γ is larger than 0.5, the postspinel phase viscosity is applied. We will consider different Clapeyron slope from 0 to −3.5 MPa/K in our models to test its effect. Previous studies have demonstrated that the phase change dynamics is mainly controlled by the Clapeyron slope and density change of the phase change, while other phase change parameters are less important (e.g., Christensen & Yuen, 1985; Zhong & Gurnis, 1994).

Mantle viscosity in our models is both depth- and temperature-dependent and the nondimensional form is

$$\eta(T, r) = \eta_r(r)\exp[E(0.5 - T)], \tag{11}$$

where $\eta_r(r)$ is the depth-dependent prefactor and E is the nondimensional activation energy. In our models, $\eta_r(r)$ is chosen such that a viscosity increase with depth by a factor of β occurs at either 670- or 1,000-km depth with β equal to 100 (Figure S1), which is broadly consistent with the geoid studies (e.g., Hager & Richards, 1989; King, 1995; Mitrovica & Forte, 2004; Rudolph et al., 2015). The lower mantle $\eta_r(r)$ is 2. Note that the dimensional viscosity depends on reference viscosity η_0 and hence Ra. The Ra in most cases of this study are 5×10^7, and the corresponding lower mantle viscosity is ~2.5×10^{22} Pa·s by using parameters in Table 2. The nondimensional activation energy E is 9.21 (i.e., corresponding to dimensional value of 191 KJ/mol if parameters in Table 1 are used) in most cases that could result in a total viscosity contrast of 10^4.

Some cases in this study include a weak layer below the phase change boundary, which plays an important role in producing horizontally deflected slabs in the transition zone as demonstrated in MZ18. This weak layer is motivated by mineral physics and geoid modeling studies that suggest significant viscosity reduction associated with the phase change

(Karato, 2008;Mitrovica & Forte, 2004 ; Panasyuk & Hager, 1998). This weak layer is defined using phase function Γ. When $\Gamma < 0.5$, the mantle viscosity is the same as that in the transition zone. However, for $0.5 < \Gamma < 0.99$, the mantle is considered in superplastic postspinel phase, and its viscosity prefactor is reduced. The effective thickness of viscosity reduction due to this weak layer is ~60 km. For $\Gamma > 0.99$, the normal post-spinel phase viscosity is applied. The resulting viscosity structure is similar to that in some geoid modeling studies (Mitrovica & Forte, 2004; Panasyuk & Hager, 1998).

2.3. Boundary and Initial Conditions and Numerical Models

We use time-dependent plate motions as surface velocity boundary conditions, while the CMB is free-slip, similar to previous studies (e.g., Bunge et al., 1998; McNamara & Zhong, 2005). The surface temperature is prescribed as a constant 0, while the CMB has either a thermally insulating boundary condition or isothermal boundary condition with constant 1 (Figure S1). Contrary to the isothermal CMB, the insulating CMB prevents thermal upwelling plumes from being generated so that our models can concentrate on evolution of subducted slabs, as used in MZ18. The insulating CMB boundary condition may be justified given that our models only cover relatively short geological time periods (65–200 Myr). However, we also use isothermal boundary conditions in this study to examine the possible dynamical interplay between upwelling plumes and the downwelling slabs.

The initial mantle temperature below the lithosphere is 0.52 (or 1,300 °C) everywhere except for near the CMB in cases with isothermal boundary condition. For the thermochemical cases, the initial nondimensional averaged temperature in the lowermost lower mantle is from previous long-duration case (Zhang et al., 2010; Li & Zhong, 2017; Figure S1). For most cases, the initial temperature in oceanic lithosphere is calculated from a plate model (Turcotte & Schubert, 2014) based on lithospheric ages (Müller et al., 2013) at the beginning of model calculations. The initial nondimensional temperature for continental lithosphere increases linearly from 0 at the surface to 0.52 at 150-km depth. Most of our model calculations are initiated at 65, 130, or 200 Ma using plate motion history from Seton et al. (2012), and the initial ages of oceanic lithosphere at 65, 130, or 200 Ma are from Müller et al. (2013). To test the effects of different plate motion history, we also use plate motion and oceanic lithosphere age models from Müller et al. (2016). We also perform calculations that initiated at 458 Ma in which the plate motions from 458 to 220 Ma are from Zhang et al. (2010), from 220 to 200 Ma are from the Seton et al. (2012) at 200 Ma, and from 200 Ma to present day are from Seton et al. (2012). For these longer time duration models, because the oceanic age and plate boundary models are not well constrained, the initial lithosphere temperature is simply taken from the horizontal averaged temperature from the case initiated at 200 Ma.

Governing equations (1)–(4) with the initial and boundary conditions are solved using CitcomS (Zhong et al., 2000, 2008) on a parallel computer Yellowstone and Cheyenne operated by National Center for Atmospheric Research. For most cases, we use a mesh with $12 \times 128 \times 128 \times 80$ grids and employ grid refinements near the surface, the phase transition, and CMB in the radial direction. With this grid, the models have a horizontal resolution of 50 km at the surface and 30 km near the CMB. Our numerical resolution tests show that the main results from this study are well resolved.

2.4. Quantifications of Models

The quantitative comparisons between different models are performed in a spherical harmonic domain, by following the method by Becker and Boschi (2002). For a field (e.g., convective temperature field at a given depth) with spherical harmonic expansion of coefficients $\{a_{lm}, b_{lm}\}$ at degree l and order m, its spectral power at degree l is

$$\sigma_l^2 = \frac{1}{2l+1} \sum_{m=0}^{l} \left(a_{lm}^2 + b_{lm}^2 \right). \tag{12}$$

The root-mean-square (RMS) power of the field is

$$\delta v_{RMS} = \frac{1}{\sqrt{4\pi}} \sigma_{RMS} = \sqrt{\frac{1}{4\pi} \sum_{l=1}^{l_{max}} (2l+1)\sigma_l^2} = \sqrt{\frac{1}{4\pi} \sum_{l=1}^{l_{max}} \sum_{m=0}^{l} \left(a_{lm}^2 + b_{lm}^2 \right)}. \tag{13}$$

For most models, we only include degrees $l = 1$–20 in the RMS power δv_{rms} calculations.

We define the RMS power for a single degree l as

$$\delta v_{RMS}^l = \frac{1}{\sqrt{4\pi}}\sigma_{RMS} = \sqrt{\frac{1}{4\pi}\sum_l (2l+1)\sigma_l^2} = \sqrt{\frac{1}{4\pi}\sum_l \sum_{m=0}^l (a_{lm}^2 + b_{lm}^2)}. \tag{14}$$

The correlation between two different fields with spherical harmonic expansions $\{a_{lm}, b_{lm}\}$ and $\{c_{lm}, d_{lm}\}$ at certain degree l is

$$r^l = \frac{\sum_{m=0}^l (a_{lm}c_{lm} + b_{lm}d_{lm})}{\sqrt{\sum_{m=0}^l (a_{lm}^2 + b_{lm}^2)}\sqrt{\sum_{m=0}^l (c_{lm}^2 + d_{lm}^2)}}. \tag{15}$$

It should be noted that statistical significance of degree correlation r^l depends on degree l (Eckhardt, 1984). For example, for two degree-1 structures to correlate at the 95% confidence level, r^1, is required to be 0.95, while for degree-20 structures, $r^{20} = 0.31$, would achieve the same level of correlations.

The total correlation from degree l_{min} to degree l_{max} is

$$r_{l_{min}-l_{max}}^{tot} = \frac{\sum_{l=l_{min}}^{l_{max}}\sum_{m=0}^l (a_{lm}c_{lm} + b_{lm}d_{lm})}{\sqrt{\sum_{l=l_{min}}^{l_{max}}\sum_{m=0}^l (a_{lm}^2 + b_{lm}^2)}\sqrt{\sum_{l=l_{min}}^{l_{max}}\sum_{m=0}^l (c_{lm}^2 + d_{lm}^2)}}. \tag{16}$$

For simplicity, when $l_{min}=1$, we write it as $r_{l_{max}}^{tot}$.

The total weighted model correlation for all the depth z_j with a total number of layers M is

$$\left\langle r_{l_{min}}^{l_{max}} \right\rangle = \frac{\sum_{j=1}^M w_j r_{l_{min}-l_{max}}^{tot}(z_j)}{\sum_{j=1}^M w_j}, \tag{17}$$

where $w_j = (R - z_j)^2$ is the weighting factor that considers the effect of volume and R is the Earth's radius. For $l_{min} = 1$, we write the total weighted correlation as $\langle r_{l_{max}} \rangle$. The nonweighted model correlation is the same as weighted model correlation except that w_j equals 1. For seismic tomographic models, we use 28 layers in total with a uniform spacing of 100 km starting from 100- to 2,800-km depths. We may also compare only a subset of the 28 layers. When comparing our convection models with seismic tomographic models, for structure in each of the 28 layers in seismic models, we use convective structure in the nearest layer from the 80 layers in our convection models to compute correlations.

When comparing tomographic and convection models, we scale the temperature anomalies in convection models into S wave anomalies. Temperature anomalies are defined as

$$\delta T = T - T_{ave}(r), \tag{18}$$

where $T_{ave}(r)$ is the horizontally averaged temperature at radius r.

We first convert the temperature anomalies at different depth into density perturbation $\delta\rho/\rho$ in percentage (%)

$$\delta\rho/\rho = -\alpha\delta T \times 100\%, \tag{19}$$

Then we scale $\delta\rho/\rho$ into S wave anomalies $\delta v_s/v_s$ by the conversion factor $\wedge$:

$$\wedge = \frac{d\ln v_s}{d\ln\rho} = \frac{\delta v_s/v_s}{\delta\rho/\rho}. \tag{20}$$

Here we use a conversion factor of 3.6 (Karato, 1993), as in Becker and Boschi (2002). Although using a different conversion factor would result in different RMS power δv_{rms} and the conversion factor might be more complex and depth-dependent (e.g., Karato & Karki, 2001; Simmons et al., 2009; Simmons et al., 2010), the calculations of correlations would not be affected.
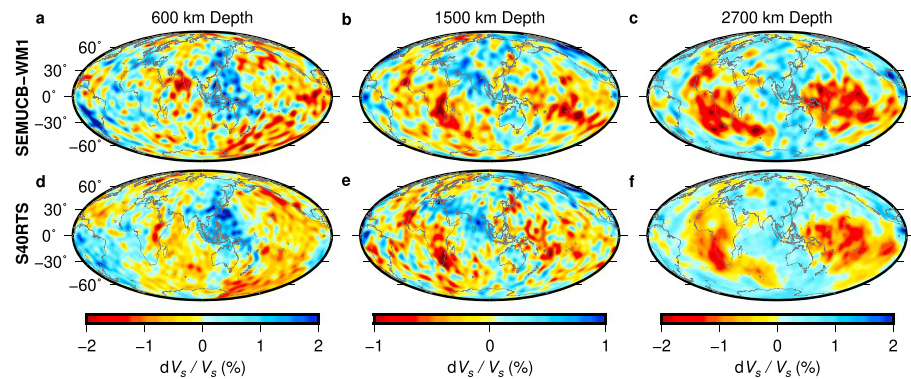
Figure 1. Map view of shear wave velocity anomalies from models (a–c) SEMUCB-WM1 and (d–f) S40RTS at 600-, 1,500-, and 2,700-km depths.

3. Results

In this section, we present results of mantle convection models with plate motion history imposed as surface boundary condition and their comparisons with seismic tomographic models. In total, 22 convection cases are computed (Table 2) to explore the effects of different model parameters including the Clapeyron slope of the spinel-to-postspinel phase change, model time duration, CMB boundary conditions (i.e., insulating versus isothermal condition), chemical heterogeneities, mantle viscosity structure (i.e., viscosity layering at 1,000-km depth), and Rayleigh number. The first four out of these 22 cases were originally presented in MZ18, and correlations analyses for these four cases are also included in this study.

3.1. Comparisons Between Different Seismic Tomographic Models

Before comparing our mantle convection models with seismic models, we first quantify correlations among different global seismic models including *S* wave tomography models SEMUCB-WM1 (French & Romanowicz, 2014) and S40RTS (Ritsema et al., 2011), *P* wave tomography model GAP_P4 (Fukao & Obayashi, 2013), and both the *P* (GyPSuMP) and *S* (GyPSuMS) wave models from GyPSuM (Simmons et al., 2010), using the same measures defined in the last section and in Becker and Boschi (2002). Note that these seismic models use different inversion techniques and data sets. S40RTS (Ritsema et al., 2011), an updated model of S20RTS (Ritsema et al., 1999), uses data of Rayleigh wave phase velocity, teleseismic body wave travel time, and normal-mode observations. SEMUCB-WM1 (French & Romanowicz, 2014) inverts the waveforms of long-period seismograms instead of travel time alone, which could provide better constraints on mantle structures, especially in the mantle transition zone and the lower mantle. GAP_P4 (Fukao & Obayashi, 2013) is a *P* wave travel time tomographic model and takes the finite-frequency effect into account. GyPSuM (Simmons et al., 2010) is a joint inversion model of *P* wave, *S* wave, and geodynamic observations that include gravity, divergence of the plate motion, surface dynamic topography, and excess ellipticity of the CMB.

We now present the comparisons between SEMUCB-WM1 and S40RTS. We first briefly summarize the common features presented in both models, and these features are also the most robust features that exist in nearly all the previous seismic models (e.g., Masters et al., 2000). The large-scale slab and LLSVP structures are similar for these two models. In the transition zone, stagnant slabs prevail in the western Pacific regions (Figures 1a, 1d, S2a, and S2b). At the middle mantle depth (e.g., 1,500 km), the circum-Pacific and Tethys slabs are evident, while seismically slow anomalies exist above the African and Pacific LLSVPs (Figures 1b and 1e). Near the CMB, the LLSVPs that are divided by circum-Pacific slabs are the dominant structures (Figures 1c and 1f). In the spherical harmonic domain, these two models correlate well at relatively low degrees ($l < 20$) or long wavelengths, and the total weighted correlations from degrees 1 to 8, $<r_8>$, and from degrees 1 to 20 $<r_{20}>$ are 0.80 and 0.69 (Figures 2 and 3), respectively. For higher degrees ($l > 20$), the correlations between these two models are generally much worse (Figure 2a). Thus, the short-wavelength structures in the tomographic models should be treated with caution.
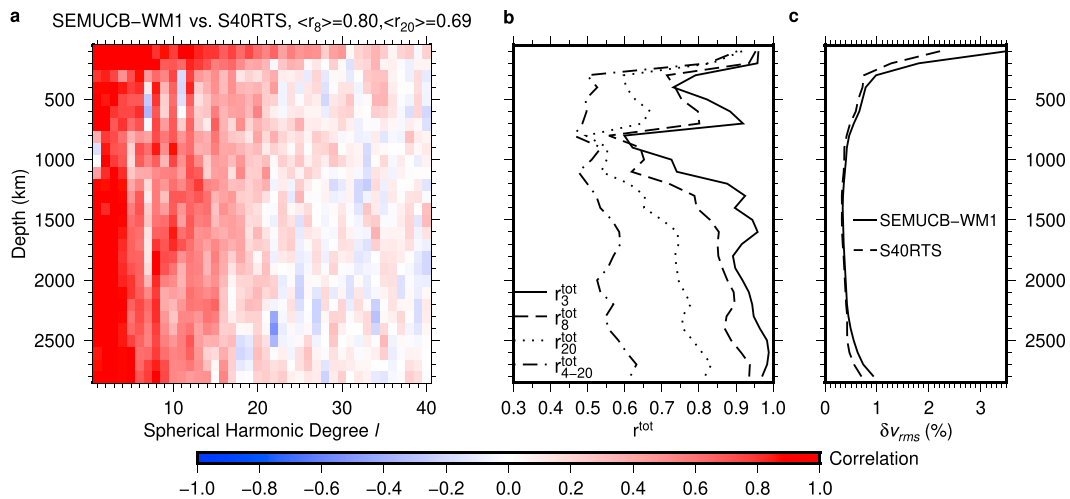
Figure 2. Comparisons between seismic models SEMUCB-WM1 and S40RTS. (a) The degree correlation between these two models at different depths. (b) The total correlations r^{tot}_3 (solid line), r^{tot}_8 (dashed line), r^{tot}_{20} (dotted line), and r^{tot}_{4-20} (dash-dotted line) at different depths. (c) The RMS power δv_{rms} (%) at different depths. The solid line is for SEMUCB-WM1 and the dashed line is for S40RTS.

The correlation between these two models is also depth dependent and is generally better near the surface and CMB (Figures 2a and 2b). The worst correlation is at ~800–1,100-km depths (Figures 2a and 2b) where the existence of stagnant lower mantle slab structures is debated (e.g., Goes et al., 2017; MZ18). Noticeably, the correlation is significantly worse at degrees 7 and 11 in the upper mantle and mantle transition zone, possibly reflecting the difference in stagnant slab structure in the transition zone between the models. For 800–1,100-km depth range, the correlation is relatively poor even at degrees 1 and 5 (Figures 2a and 2b). While this leads to significantly reduced total correlation at long wavelengths (from degrees 1 to 3 or to 8) over this depth range (Figure 2b), the total correlation at intermediate wavelengths (from degrees 4 to 20) does not show significant change compared with other depths (Figure 2b). The RMS powers δv_{rms} are nearly the same for both models in the middle mantle range but are larger in model SEMUCB-WM1 near the surface and CMB (Figure 2c). As in previous models, degree-2 power is the strongest at nearly all depths (Figure S3).

Similar to the comparison between SEMUCB-WM1 and S40RTS, the total correlations are relatively high for long-wavelength structures for all the seismic tomographic models considered in this study. The total weighted correlation $<r_8>$ ranges from 0.80 (S40RTS versus SEMUCB-WM1; Figure 3a) to 0.62 (GAP_P4 versus GyPSuMP), and $<r_{20}>$ ranges from 0.69 (S40RTS versus SEMUCB-WM1; Figure 3a) to 0.56 (SEMUCB-WM1 versus GyPSuMP; Figure 3a). In general, S wave anomaly models correlate better with SEMUCB-WM1 (also a S wave model) than P wave anomaly models with SEMUCB-WM1, as expected. Only considering the fast anomalies (i.e., slab structures) does not change the correlation results much (Figures 3a and 4a). The power spectra are similar for all the tomographic models, in which degree 2 power dominates (Figure S3). All the S wave models have similar RMS powers δv_{rms} in the middle mantle, while the largest differences appear near the boundary layers. This is also true for the P wave models, but P wave models have much smaller δv_{rms} than S wave models across the mantle (Figure S3).

The high correlations for long- and intermediate-wavelength structures (e.g., for l up to ~16 in Figure 2a) among different seismic models suggest the robustness of these structures with possible exceptions at ~1,000-km depth. Therefore, interpretation of these robust structures is an important goal for studies of global mantle dynamics such as ours presented here. In our study we compare convection model results mostly with SEMUCB-WM1, but our general conclusions are insensitive to seismic models given that we are concerned mostly with robust structures.

3.2. Slab Structures From Convection Models With Insulating CMB
3.2.1. Effects of the Weak Layer and the Phase Change
We first present our standard model Case 1, which is Case 4 in MZ18. We only briefly introduce the case here. This case starts from 130 Ma, the CMB is thermally insulated, the Clapeyron slope for the spinel-to-
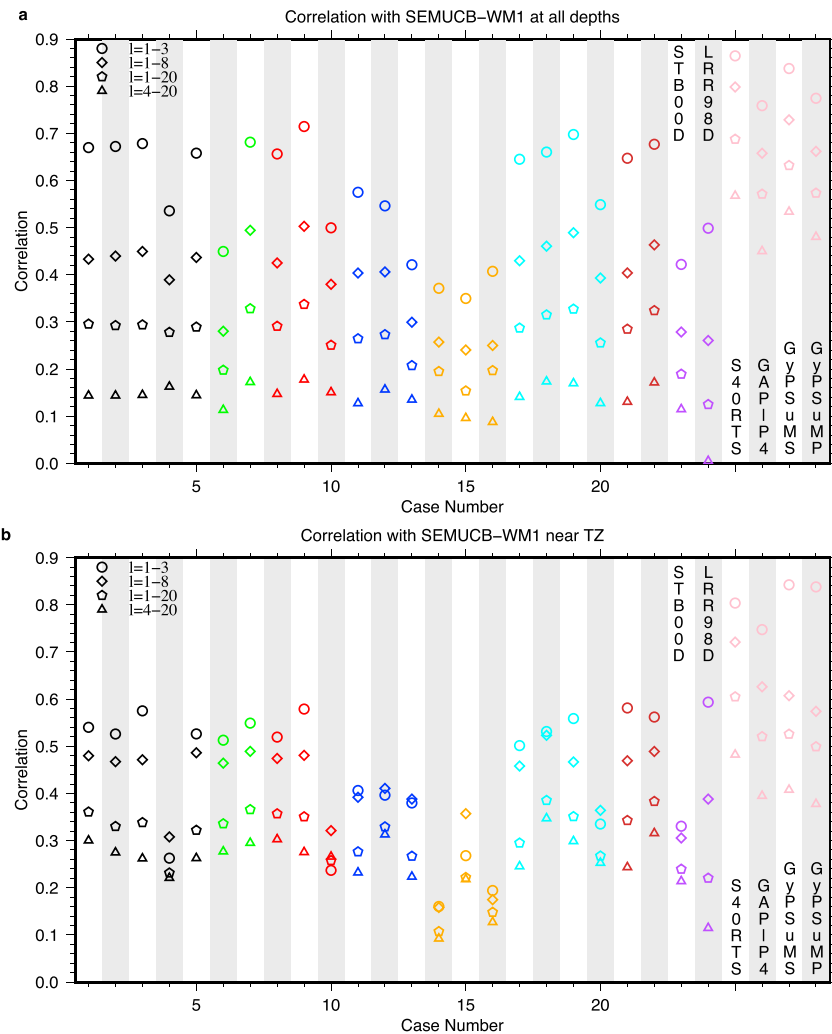
Figure 3. The total weighted correlations between different models and seismic model SEMUCB-WM1 for structures at (a) all depths and (b) between 600- and 800-km depths. Cases 1 to 22 are listed in Table 2. Also included are the correlations with SEMUCB-WM1 for the slab models stb00d (Steinberger, 2000) and lrr98d (Lithgow-Bertelloni & Richards, 1998; Ricard et al., 1993), seismic models S40RTS (Ritsema et al., 2011), GAP_P4 (Fukao & Obayashi, 2013), GyPSuMS, and GyPSuMP (Simmons et al., 2010). The circles, diamonds, pentagons, and triangles represent the correlations for l from 1 to 3, from 1 to 8, from 1 to 20, and from 4 to 20, respectively. Different colors represent different groups of models: the black ones are for Cases 1 to 5 which are mainly about the effects of Clapeyron slope and the weak layer beneath the mantle transition zone, the green ones are for Cases 6 and 7 which are mainly about the effects of duration of imposed plate motion history, the red ones are for Cases 8 to 10 which are mainly about the effects of thermochemical piles, the blue ones are for Cases 11 to 13 which are mainly about the effects of isothermal CMB boundary condition for purely thermal models, the orange ones are for Cases 14 to 16 which are mainly about the effects of Ra, the cyan ones are for Cases 17 to 20 which are mainly about the effects of the 1,000-km discontinuity, the brown ones are for Cases 21 and 22 which mainly about the effects of using different plate motion models, the purple ones are for previous slab-only models stb00d and lrr98d, and the pink ones are for different seismic models.

postspinel phase transition is -2.0 MPa/K, and there is a reduced viscosity layer beneath the phase boundary. As discussed in MZ18, not only the lower mantle seismic slabs but also the stagnant slab structures in the transition zone are well reproduced in this model (Figures 1, 5, and S2). Specifically, in the lower mantle, this case successfully reproduces the Farallon and Tethys slabs, and slabs in the eastern Asia, the Central and Southern Americas (Figures 5b and 5c). As to be demonstrated later, although these model lower mantle slab structures are similar to those in previous convection models, they also represent a significant improvement (e.g., Bunge & Grand, 2000; Lithgow-Bertelloni & Richards, 1998; Liu et al., 2008; Ricard et al., 1993). In the mantle transition zone of the Northern Honshu, Calabria, Bonin-
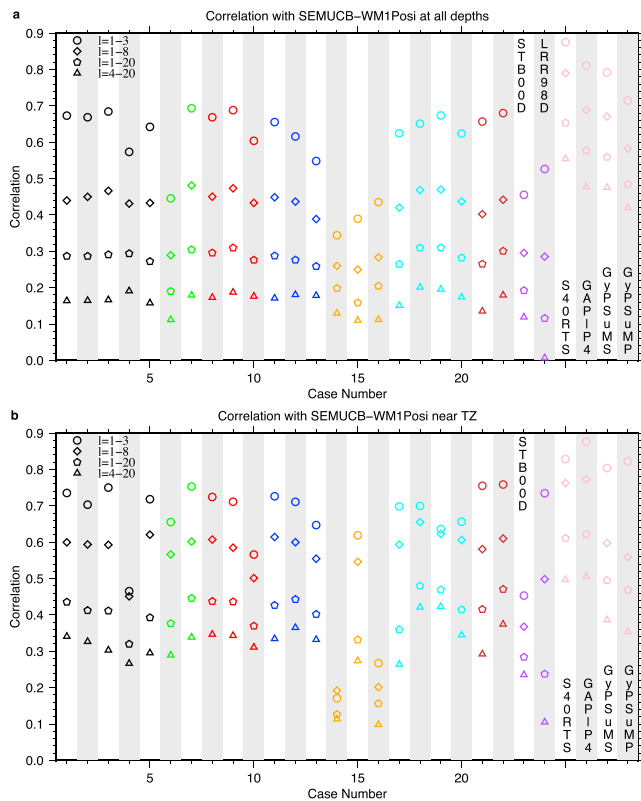
Figure 4. Same as Figure 3 except that all the seismic models (SEMUCB-WM1, S40RTS, GAP_P4, GyPSuMS, and GyPSuMP) include only fast anomalies and all the convection models include only negative temperature anomalies.

Mariana, Tonga, and Western Java subduction zones, Case 1 successfully explains the long, horizontally deflected stagnant slabs (Figures 5a, S2, and MZ18's Figures 1, 2, and S4) that previous convection models fail to explain.

At long wavelengths ($l \leq 3$) the correlations between Case 1 and SEMUCB-WM1 are high across the mantle (Figures 6a and 6b). At intermediate to short wavelengths ($l = 4$–20), high correlations between Case 1 and SEMUCB-WM1 occur in the upper mantle and the uppermost lower mantle, but the correlations decrease significantly to either negative or zero at depths below 1,000 km in the lower mantle (Figures 6a and 6b). This suggests that it remains a significant challenge for this type of mantle convection models to consistently simulate mantle seismic structures below 1,000-km depth at these wavelengths (i.e., <~10,000 km). Although the correlations for l from 1 to 8 or 20 are significant in the lower mantle, they mostly result from the good correlations from degrees 1 to 3. The total weighted correlations $\langle r_8 \rangle$ and $\langle r_{20} \rangle$ between Case 1 and SEMUCB-WM1 are 0.43 and 0.30, respectively. If we compare only seismically fast anomalies (i.e., slabs) in SEMUCB-WM1 with Case 1, $\langle r_8 \rangle$ and $\langle r_{20} \rangle$ are improved to 0.48 and 0.31, respectively (Figures S4a and S4b).

Better correlations are exhibited at four different depth ranges (Figures 6a and 6b). The first depth range is near the surface at ~100-km depth where the mid-ocean ridge structures are well reproduced in our convection model (e.g., Li et al., 2016; Zhang et al., 2012). The second and third depth ranges with better correlations are around the mantle transition zone to 800-km depths and in the middle mantle at 1,400–1500-km depths, respectively, reflecting the fact that the stagnant and penetrated slab structures are well reproduced. The fourth depth range is in the lower-most lower mantle at 2,600–2,800-km depths where the slabs pile up above the CMB (Figure 5c). The smallest correlation in r_8^{tot} is at ~200–300-km depths (Figure 6b). At this depth range, the seismic velocity anomalies may be significantly affected by composition (e.g., seismically fast continental roots) and seismic anisotropy (e.g., Deschamps et al., 2001; Jordan, 1975; Ritzwoller et al., 2004), while in our isochemical convection models (e.g., Case 1), it is the negative temperature that dominates the slab (i.e., fast seismic velocity) structure. We found that the correlations at these depths improve significantly if we replace mantle structure in continental cratonic regions with seismic structure (Figures S5d and S5e versus Figures 6a and 6b). In re-computing the correlations here, we define the continental cratonic regions as those in the top 300 km with $\delta v_s / v_s > 2\%$ in SEMUCB-WM1 and convert the seismic anomalies into temperature anomalies using the conversion method in equations (19) and (20) (Figures S5a–S5c). The improved correlations suggest nonthermal contribution to the seismic structure in continental cratonic regions.

The overall distribution and amplitude of δv_{rms} (Figure 6c) in Case 1 are very similar to that in SEMUCB-WM1. The main difference is at the lowermost lower mantle where due to the insulating boundary condition at the CMB in Case 1 that excludes thermal plumes or thermochemical piles, δv_{rms} in Case 1 is significantly reduced. The effects of plumes or thermochemical piles will be discussed in section 3.3. Another difference is at ~670-km depth where δv_{rms} in Case 1 has a local maximum due to stagnant slabs. It should be noted that in the δv_{rms} calculations, we only consider the temperature-related density anomalies and do not take the phase change density into account. Also, if we only consider fast velocity anomalies in SEMUCB-WM1, the δv_{rms} would be reduced nearly by a half (Figure S4c).

Case 2 differs from Case 1 only by excluding the phase transition and the weak layer. This case is the Case 1 in MZ18. Although Case 2 also reproduces the lower mantle seismic slab structures (Figures 5e and 5f), it fails to reproduce the stagnant slab structures in the transition zone (Figures 5d and S2). The correlations of Case 2 with SEMUCB-WM1 at different depths at different wavelength bands are similar to those for Case 1 (Figures 3a, 6a, 6b, 6d, and 6e). The main difference is at around 600–800-km depths for
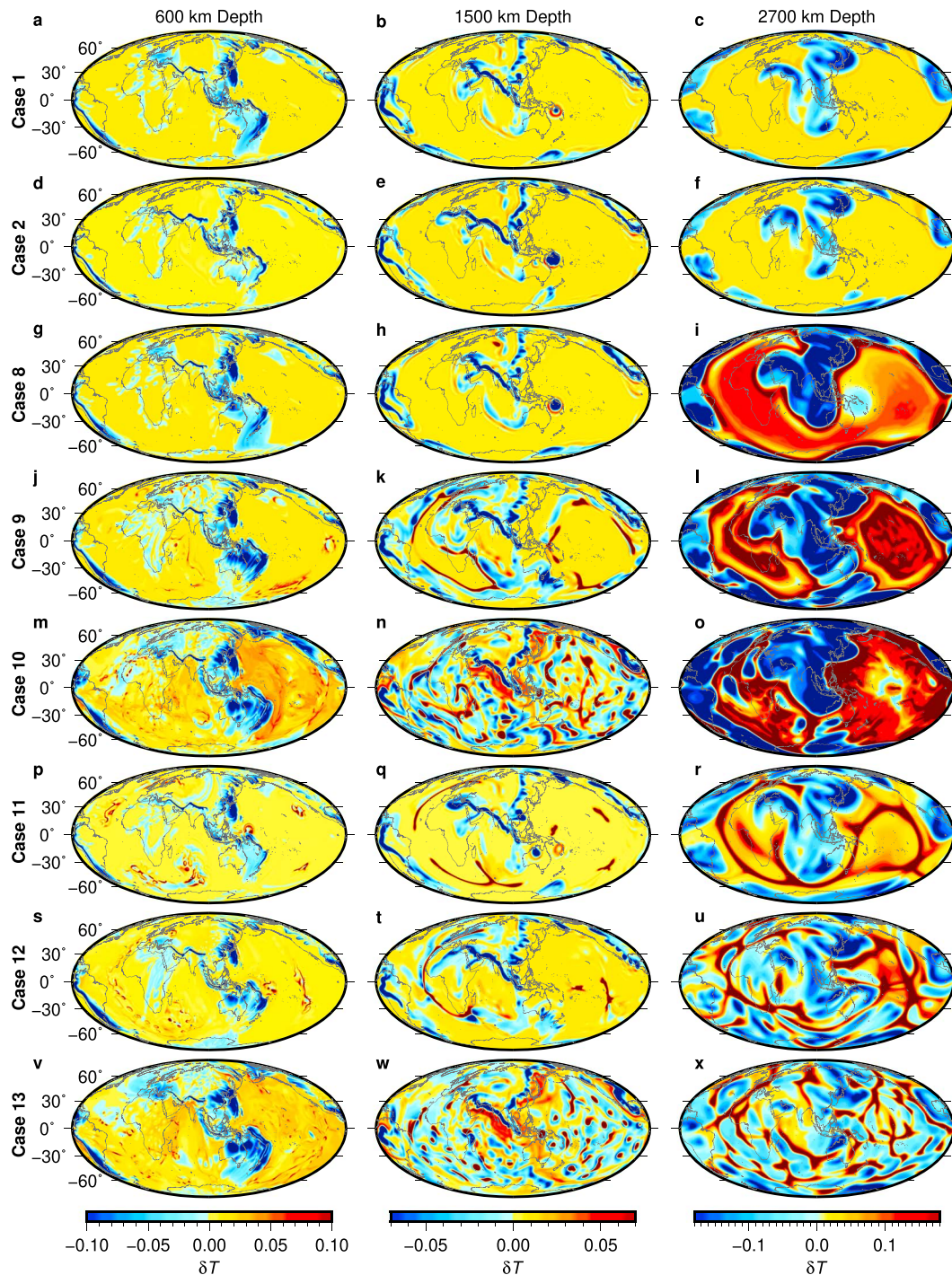
Figure 5. Present-day dimensionless temperature anomalies of eight different convection models at 600-, 1,500-, and 2,700-km depths. (a–c, d–f, g–i, j–l, m–o, p–r, s–u, and v–x) Cases 1, 2, 8, 9, 10, 11, 12, and 13, respectively. The left, middle, and right columns are for 600-, 1,500-, and 2,700-km depths, respectively. Note that the different color bars are used for different depths.

intermediate to short wavelengths (i.e., $l = 4$–20 and 1–20). The correlations of Case 1 with SEMUCB-WM1 at these two wavelength bands at 600–800-km depths are better than that of Case 2 that fails to reproduce the stagnant slabs (Figures 3b, 6b, and 6e), although the difference in correlations does not appear as large as the transition zone slab structures would suggest (Figures 5a, 5d, and S2). Also, if we only consider the fast
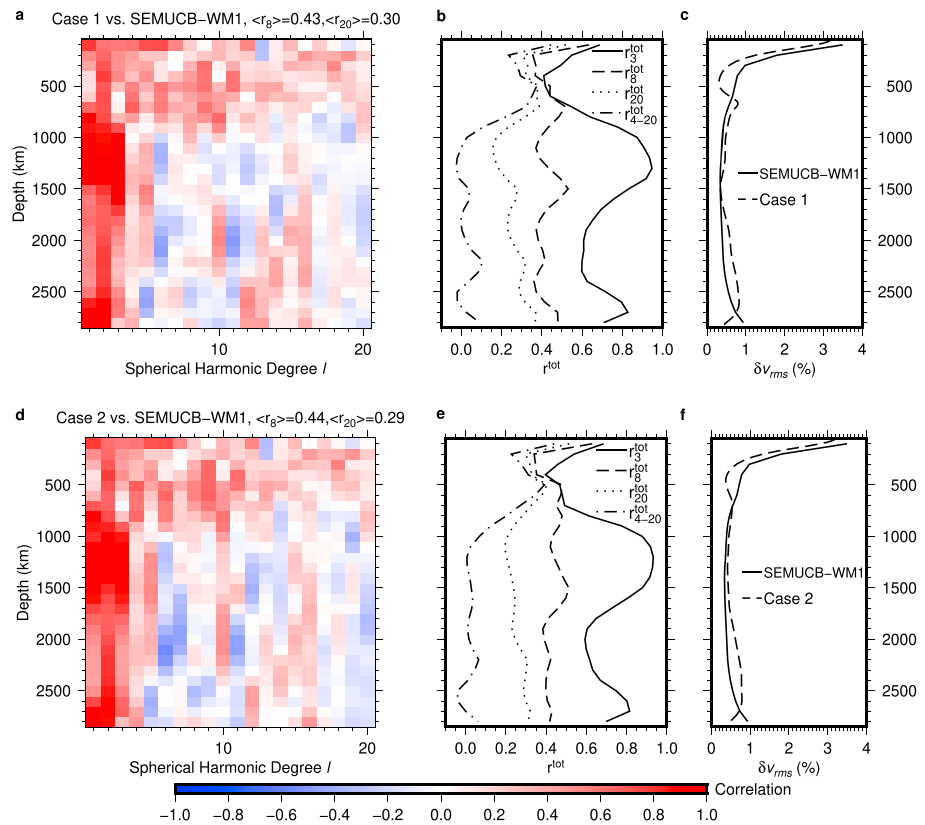
Figure 6. (a) The degree correlation between SEMUCB-WM1 and Case 1 at different depths. (b) The total correlations between SEMUCB-WM1 and Case 1 at different depths for different wavelength bands: r^{tot}_3 ($l = 1$–3, solid lines), r^{tot}_8 ($l = 1$–8, dashed lines), r^{tot}_{20} ($l = 1$–20, dotted lines), and r^{tot}_{4-20} ($l = 4$–20, dash-dotted lines). (c) The RMS power δv_{rms} (%) for SEMUCB-WM1 (solid line) and Case 1 (dashed line) at different depths. (d–f) Counterparts of Figures 6a–6c, respectively, for Case 2.

anomalies in SEMUCB-WM1, the correlations of Cases 1 and 2 with SEMUCB-WM1 are all improved, but the main conclusions remain unchanged (Figures S4 and 4).

We may also compare Cases 1 and 2 by quantifying their correlations. The total weighted correlations between these two cases are high (Figures S6a and S6b), and $<r_8>$ and $<r_{20}>$ are 0.94 and 0.90, respectively, indicating that Cases 1 and 2 are largely similar. The correlations are nearly perfect for degrees up to 50–60 above 400-km depth. However, the correlations decrease with increasing degrees (or decreasing wavelengths) and increasing depth (Figure S6a). In particular, the first local minimum in correlation between these two models is at ~600-km depth, and the weakest correlation occurs at ~1,500-km depth (Figure S6b). This is due to the fact that in Case 1 some slabs have been temporarily stopped (for 20–30 Myr) and horizontally deflected (i.e., stagnant) at 670-km depth due to the phase change and have reached to different depths in the lower mantle than that from Case 2 (Figures 5b and 5e; see MZ18). The correlations are improved at >1,800-km depths, because the slabs in Case 1 eventually sink into the lower mantle and pile up above the CMB, like that in Case 2. The RMS power δv_{rms} for Case 1 is noticeably higher at ~670-km depth but lower at ~1,500 km than that for Case 2, reflecting the difference in slab structures at these depths between these two cases. However, δv_{rms} is nearly identical for these two cases at other depths (Figure S6c).

We now compare these two cases at ~600-km depths in detail. The RMS powers δv_{rms}^l for structures at this depth (Figure S7b) show that the power contrast between relatively low degrees ($l \lesssim 20$) and high degrees ($l \gtrsim 20$) is much larger in Case 1 than Case 2. This is because the stagnant slabs in Case 1 represent longer-wavelength structures (~1,000 km) compared with directly sinking slabs (~200 km in width) in Case 2 (Figures 5a, 5d, and S2). For example, in Case 1 stagnant slabs appear in the transition zone in most

regions across the north-western Pacific, contributing to the power increase of long and intermediate wavelengths of $l \lesssim 20$. It is interesting to note that model SEMUCB-WM1 also shows a large power contrast between relatively long wavelengths and short wavelengths at this depth, similar to that in Case 1 (Figure S7b). However, at 400- and 1,000-km depths (i.e., above and below the transition zone), Cases 1 and 2 appear to have similar power distribution (Figures S7a and S7c) with much smaller power contrast between long wavelengths and short wavelengths.

Cases 3 and 4 differ from Case 2 only in that they have the phase transition with Clapeyron slope of −2.0 and −3.5 MPa/K, respectively (Table 2). Case 3 differs from Case 1 only in excluding the weak layer and differs from Case 2 only in including the phase boundary. The slab structures of Case 3 are nearly identical to Case 2 and the stagnant slabs are not well reproduced in neither of Cases 2 and 3 (Figure S2). The total weighted correlations between Case 3 and SEMUCB-WM1 are similar to those between Case 1 and SEMUCB-WM1 for different wavelength bands ($l = 1–3$, 1–8, 1–20, and 4–20; Figure 3a). For structures between 600- and 800-km depths, although the correlation for long wavelengths ($l = 1–3$) in Case 3 is noticeably larger than that of Case 1, at larger degrees of $l = 1–8$, 1–20, and 4–20 where intermediate and short wavelengths are included, the correlations of Case 3 are all smaller than those of Case 1 (Figure 3b), confirming that Case 3 does not fully capture the stagnant slab structures ($l = 4–20$) as well as Case 1. For Case 4, with unrealistically large Clapeyron slope of −3.5 MPa/K, there are widespread stagnant slabs in the mantle transition zone that are inconsistent with seismic models (see MZ18). Both the total weighted correlations and those near the transition zone depths for all the wavelength bands between Case 4 and SEMUCB-WM1 are much worse than those of Case 1 (Figure 3).

In order to evaluate how the weak layer beneath the transition zone affects slab morphology, we computed Case 5 which is identical to Case 1 except without the phase change and differs from Case 2 only in having a weak layer. Without the phase change, the low-viscosity weak layer fails to produce the stagnant slab structures (Figures S8a, S8d, and S8e) as Case 1 does. Slabs tend to penetrate into the lower mantle (Figures S8a–S8g) more easily compared with Case 2 in which no weak layer is employed. Thus, both the phase change and the weak layer are crucial in reproducing the stagnant slab structures in the transition zone. The overall correlations of Case 5 with SEMUCB-WM1 are comparable with those of Case 2 and are slightly worse than those of Case 1, particularly when short-wavelength structures are considered (Figure 3).

3.2.2. Effects of Time Duration of Imposed Plate Motion on Slab Structures

We now present Cases 6 and 7 that are identical to Case 1 except that these two models are computed for the last 65 and 200 Myr, respectively, differing from 130 Myr in Case 1. With only 65-Ma plate motion history, most of the slabs have not traveled significantly beyond ~1,500-km depth into the lower mantle in Case 6 (Figures S9g, S9h, S9j, S9k, S9m, and S9n). Consequently, the correlations of Case 6 with SEMUCB-WM1 below ~1,500 km are insignificant for all the wavelength bands (Figures S10a and S10b), leading to significantly reduced total correlations compared with other cases (Figure 3a). However, the correlations above ~1,500 depth are generally similar to that of Case 1 (Figures 3b, 6a, and 6b). Also, the RMS power δv_{rms} of Case 6 is much smaller below ~1,500-km depth compared with Case 1 (Figure S10c versus Figure 6c), again suggesting that 65-Myr time duration is not long enough for the slab structures to fully develop in the lower mantle (e.g., Bunge et al., 1998).

Case 7 with 200-Ma plate motion history reproduces more slab structures that are not captured in Case 1 with 130 Ma. Especially above the CMB, significantly more slabs which are originated from more ancient subduction zones are shown in Case 7 (Figures S9k, S9l, S9n, and S9o). Therefore, the longer plate motion history in Case 7 leads to improved correlations with SEMUCB-WM1 compared to that of Case 1 (Figure 3), and $<r_8>$ and $<r_{20}>$ are 0.49 and 0.33, respectively. The main improvements, as seen in r^{tot}_8, occur at around 800–1,300- and 2,200–2,500-km depths, while at other depths the correlations are similar to Case 1 (Figures S10e and 6b). The RMS power δv_{rms} of Case 7 is only slightly larger than Case 1 in the lower mantle (Figure S10f). The improved correlations of Case 7 relative to Case 1 suggest that despite uncertainties with relatively old plate motion history (>130 Ma), the longer plate motion history (200 Ma) is still helpful in reproducing seismic slab structures in the lower mantle.

3.3. Convection Models With Isothermal CMB Condition

This section explores how isothermal CMB condition may lead to plume and thermochemical piles structures that may affect the slab structure and the correlations between convection models and seismic models.

3.3.1. Thermochemical Convection Models

The African and Pacific LLSVPs in the lowermost lower mantle may have a distinct composition compared with the ambient mantle (e.g., Garnero et al., 2016). To investigate the effect of chemical composition on the LLSVP and slab structures, we computed three different thermochemical convection models (i.e., Cases 8–10) with compositional buoyancy, similar to previous studies (e.g., McNamara & Zhong, 2005). These three cases include an isothermal CMB and a layer of intrinsically dense material above the CMB (Table 2), but otherwise are similar to Case 1. Cases 8 and 9, both with buoyancy number B of 0.2, differ only in the total model times that are 130 and 200 Myr, respectively. Case 10 has an even longer total model time of 458 Ma and a larger buoyancy number B of 0.25 to prevent the chemical piles from fully entrained (e.g., Li & Zhong, 2017; McNamara & Zhong, 2004; Zhong & Rudolph, 2015). Although thermochemical piles are generated above the CMB below the Africa and Pacific in Case 8, no plumes appear at 1,500-km depth, suggesting that more time is required for plumes to form and to ascend when thermochemical piles are presented with the lower mantle viscosity used in this case (Zhong & Rudolph, 2015). The slab structures for the present-day mantle in Case 8 are identical to Case 1 across the mantle (Figures 5a–5c and 5g–5i). The total weighted correlations $<r_8>$ and $<r_{20}>$ between Cases 8 and 1 are 0.97 and 0.96, respectively. The main difference compared with Case 1 is the two large thermochemical piles above the CMB (Figure 5i). The overall correlations of Case 8 with SEMUCB-WM1 are nearly identical to that of Case 1 at all the wavelength bands throughout the mantle perhaps except near the CMB where Case 8's correlations with the seismic model is generally better due to the presence of the thermochemical piles (Figures 3, 4, 6a, 6b, 7a, and 7b). The thermochemical piles in Case 8 also lead to increased RMS power δv_{rms} in the lowermost lower mantle, compared with Case 1 (Figures 6c, 7c, and 8a).

Case 9 with 200-Ma plate motion history has the best correlations with model SEMUCB-WM1 among all the cases in this study, and the main characteristics of both the stagnant slabs and LLSVPs structures in the seismic model are well reproduced in this case (Figures 5j–5l and S8h–S8k). At 2,700-km depth, the shapes of the African and Pacific thermochemical piles in Case 9 (Figure 5l) are nearly identical to the LLSVPs in seismic tomographic models (Figures 1c and 1f) and represent an improved match to seismic models over Case 8. The African and Pacific thermochemical piles in Case 9 (Figure 9) are also consistent with previous mantle convection models without the weak layer beneath the mantle transition zone (e.g., Bower et al., 2013; McNamara & Zhong, 2005; Steinberger et al., 2012; Zhang et al., 2010; Zhong & Rudolph, 2015). A significant portion of the Pacific and African thermochemical piles reaches ~500 km above the CMB, and their edges rise even higher height (Figure S11). Plumes are now present throughout the mantle in Case 9, and they show no simple relationship to the edges of the thermochemical piles, as demonstrated in Li and Zhong (2017). Importantly, the presence of mantle plumes and thermochemical piles does not appear to affect the slab structures in Case 9 that are similar to that in Cases 1 and 8 including stagnant slabs in the mantle transition zone and slabs in the lower mantle (Figures 5j, 5k, and 9). Compared with Case 1, the correlations between Case 9 and SEMUCB-WM1 are improved significantly at all the wavelength bands, and the $<r_3>$, $<r_8>$, and $<r_{20}>$ with SEMUCB-WM1 are 0.71, 0.50, and 0.34, respectively (Figure 3a). The improvements (e.g., r^{tot}_3 and r^{tot}_8) mainly occur at 400–800-km depth and below 2,300-km depth (Figures 7d and 7e) with the maximum r^{tot}_3 and r^{tot}_8 at 2,700-km depth that are 0.91 and 0.66, respectively. The RMS power δv_{rms} increases at all depths below 300-km depth compared with Case 1 (Figures 7f and 8a), reflecting the contributions of mantle plumes to the power (Figure 9).

With longer plate motion history of 458 Ma, Case 10 shows more plumes in the mantle: not only above the edges of the LLSVPs but also above the middle and outside of the LLSVPs (Figures 5m and 5n). The correlations of Case 10 with SEMUCB-WM1 are significantly lower than other cases (Figure 3a), particularly from 700- to 1,400-km depths and at degree 1 (Figures 7g and 7h). The reduction in correlations at degree-1 may be due to that the Pacific thermochemical pile is significantly larger in size than the African thermochemical pile near the CMB in Case 10 which causes uneven distributions of mantle plumes originated from the piles (Figure 5o). As shown in Zhang et al. (2010), the degree-1 structure is the predominant mantle structure at ~330 Ma caused by assembly of supercontinent Pangea, and has subsequently evolved into predominantly degree-2 structure with the Pacific and African thermochemical piles at the present as a result of Pangea breakup. However, the structure transition depends on model parameters including mantle viscosity, plate motion history, and chemical buoyancy number (Zhang et al., 2010; Zhong & Rudolph, 2015). With the model parameters in Case 10, the degree-1 structure remains relatively strong at the present day.
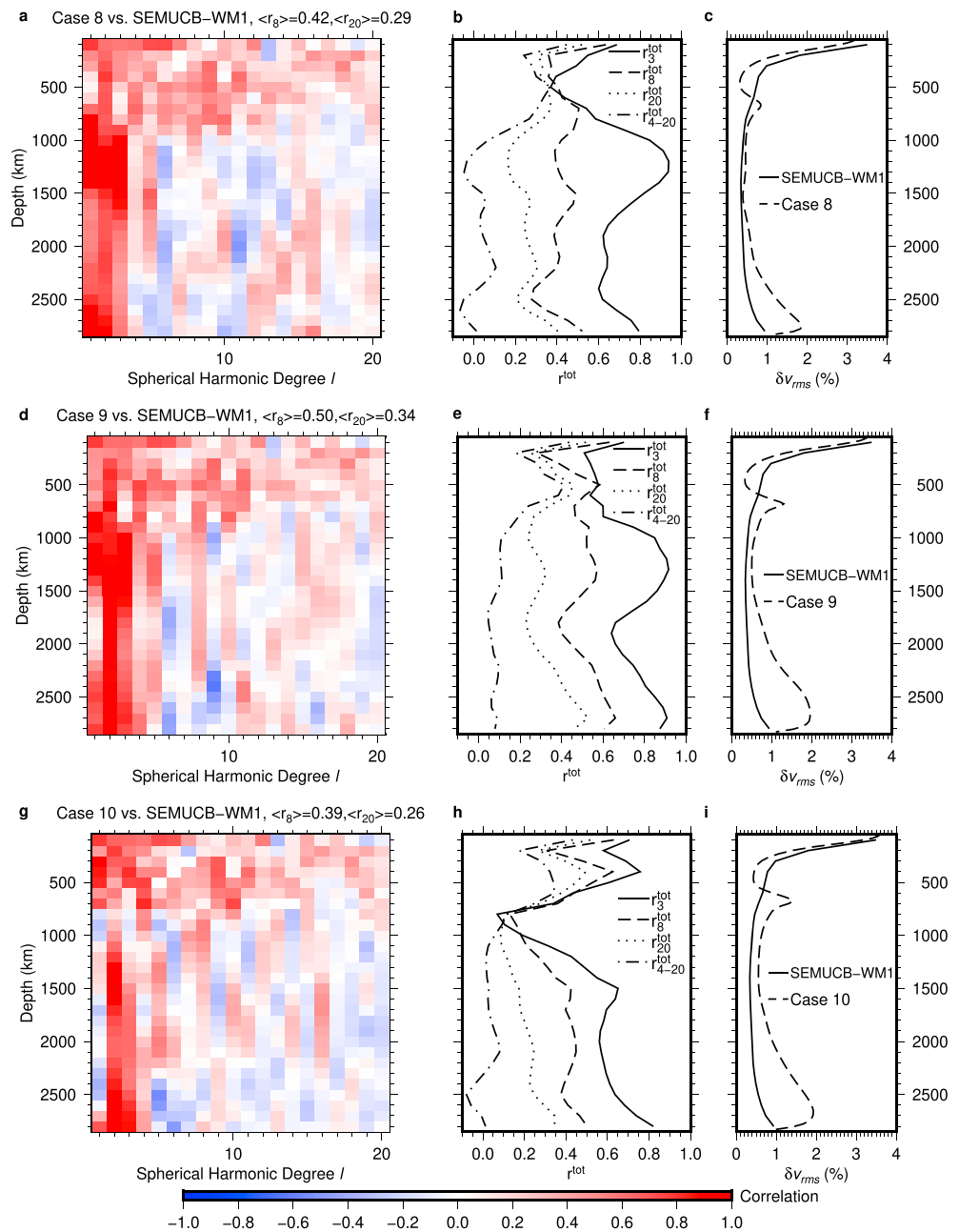
Figure 7. Same as Figure 6 but for Cases (a–c) 8, (d–f) 9, and (g–i) 10.

However, the slab structures in the mantle, especially the stagnant slabs structures in the transition zone are still nearly identical to that in Case 1 (Figures 3b, 4b, 5a, and 5m). Because the plumes locations are mainly controlled by the thermal boundary layer instability and are difficult to predict (Li & Zhong, 2017), the reduced correlations with tomographic models in models with more plumes are not so surprising. The RMS power δv_{rms} of Case 10 is nearly the same as Case 9 (Figure 8a), demonstrating that 200 Myr is a sufficiently long time for thermochemical models to fully develop mantle structures in terms of power.

3.3.2. Purely Thermal Convection Models

It is still in debate whether the LLSVPs are purely thermal or thermochemical origins (Davies et al., 2012; Zhong & Liu, 2016). We computed Cases 11–13 that are identical to Cases 8–10 except that they are isochemical models excluding chemical buoyancy (Table 2). For Case 11, at 2,700-km depth, clusters of thermal plumes are evident in the African and Pacific seismically slow anomalies regions (Figure 5r). And the
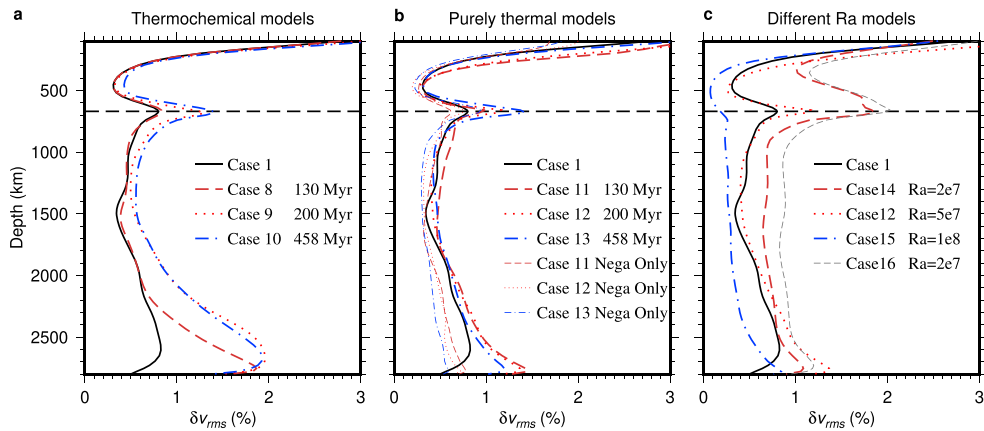
AGU
100
ADVANCING EARTH
AND SPACE SCIENCE

Journal of Geophysical Research: Solid Earth

10.1029/2019JB017918

Figure 8. The depth dependence of RMS power δv_{rms} (%) for different cases, (a) for thermochemical models: Cases 8-10; (b) for purely thermal models: Cases 11-13, and Cases 11-13 with only negative temperature anomalies (i.e., slab structures); and (c) for different Ra models: Cases 14, 12, 15, and 16. Note that in each figure, Case 1 is also shown as a reference.
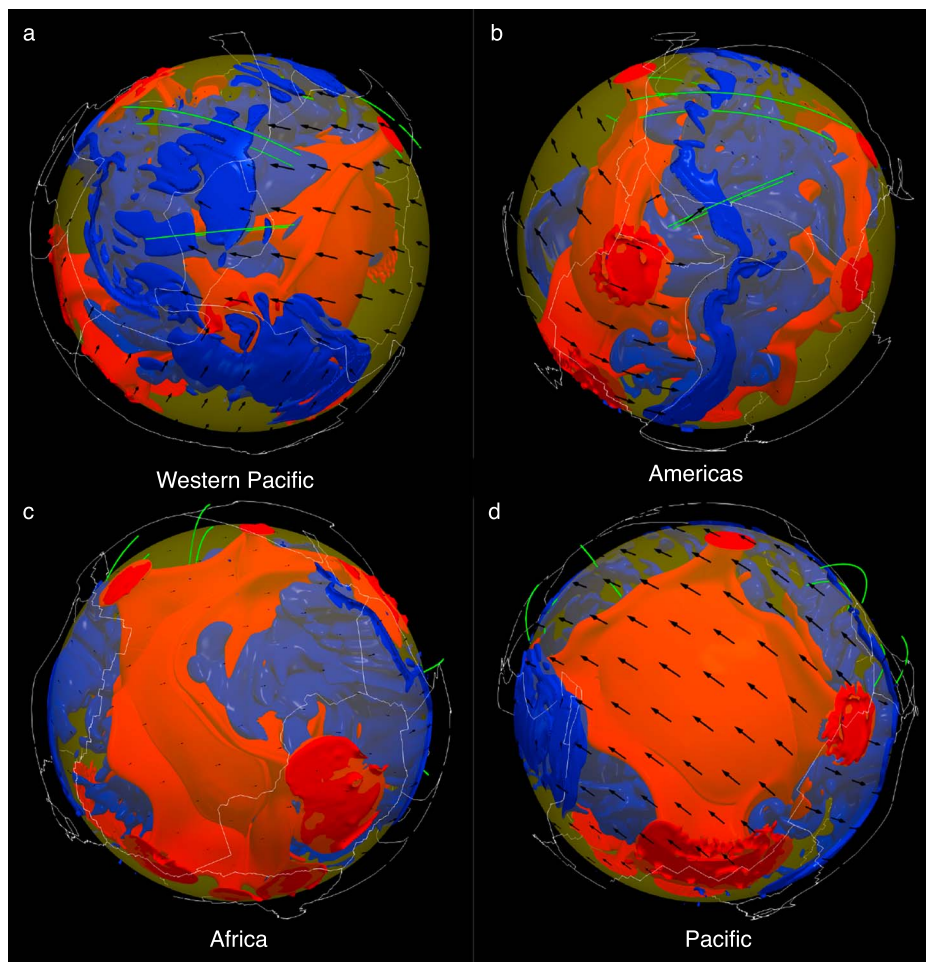

Figure 9. The 3-D perspective views of Case 9 at present day as viewed from (a) the western Pacific, (b) Americas, (c) Africa, and (d) Pacific. Blue and red surfaces are isosurfaces of dimensionless temperature anomalies of −0.05 and 0.05, respectively. The yellow transparent surface is at 670-km depth. The white lines at surface are plate boundaries at present day, the black arrows at surface are plate motion velocities, and the green lines are the four cross sections shown in Figure S8 at surface and 670-km depth.
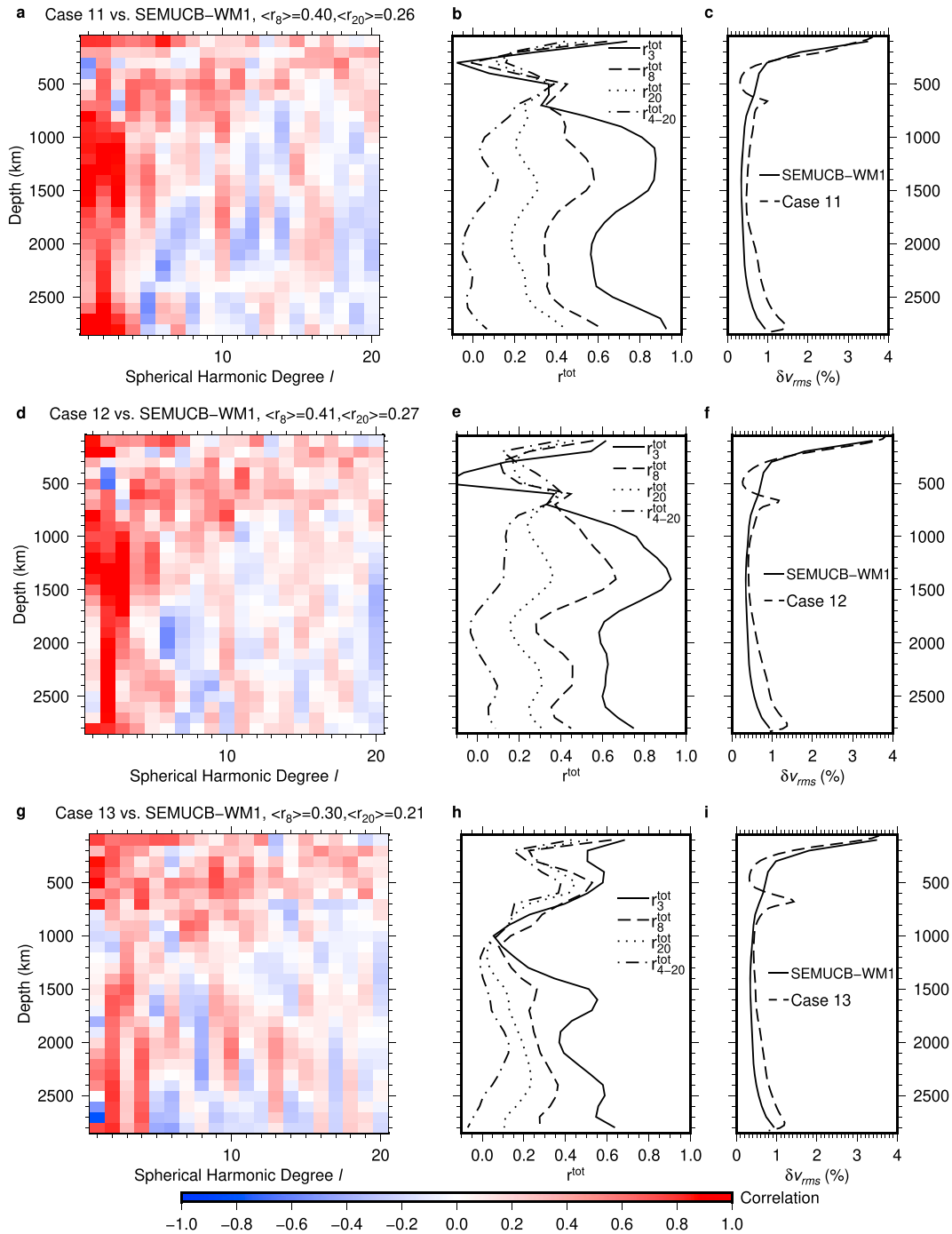
Figure 10. Same as Figure 6 but for Cases (a–c) 11, (d–f) 12, and (g–i) 13.

correlations between Case 11 and SEMUCB-WM1 at long to intermediate wavelengths ($l = 1$–3 and 1–8) are significantly improved in the lowermost lower mantle compared with those between Case 1 and SEMUCB-WM1 (Figures 6a, 6b, 10a, and 10b). The r^{tot}_3 and r^{tot}_8 between Case 11 and SEMUCB-WM1 are 0.93 and 0.62 at 2,800-km depth, which are nearly identical to the best fit thermochemical model Case 9. Therefore, it is difficult to distinguish between the purely thermal and thermochemical origins of the LLSVPs solely on the basis of correlations of mantle convection models with tomographic models in the lowermost lower mantle. This is consistent with Lassak et al. (2010) that came to a similar conclusion on the basis of long-

wavelength core-mantle boundary tomography from purely thermal and thermochemical models of the LLSVPs.

Broad mantle plumes in Case 11 are evident at ~300-km depth at the present day, as they ascend to the upper mantle and spread below the lithosphere (Figure S12h), and these plume structures cause significant reduction in correlation with seismic models in the upper mantle. Unlike in thermochemical model Case 8 that few plumes appear at 1,500-km depth (Figure 5h), it takes less time for plumes to develop and ascend through the mantle in purely thermal model Case 11, as expected. However, the spatial distribution of plumes at ~300-km depth is different from that of the slow anomalies in SEMUCB-WM1, S40RTS, and GAP_P4 (Figures S12a–S12c). This leads to significantly reduced correlations between Case 11 and SEMUCB-WM1 at 200–300-km depths, compared with Cases 1 and 8 that do not contain such plume structures (Figures 10a and 10b). However, the plume's effects on correlation appear only significant at depths less than ~700 km, because the correlations of Case 11 with SEMUCB-WM1 are similar to that of Case 1 at larger depths (Figures 10a and 10b versus Figures 6a and 6b). The slab structures in Case 11 (Figures 5p–5r) remain similar to that in Case 1 (Figures 5a–5c). This is demonstrated by the nearly identical correlations of the relatively cold structures (i.e., the slabs) in Cases 11 and 1 with the seismically fast structures in SEMUCB-WM1 (Figure 4), although the correlations between Case 11 and SEMUCB-WM1 are noticeably worse than those between Case 1 and SEMUCB-WM1 when their full structures are considered (Figure 3), indicating that it is not slab structures but plume structures that reduce the correlations in Case 11. Similar to the thermochemical cases, δv_{rms} of Case 11 in the lowermost lower mantle are larger than that of Case 1 (Figures 8b and 10c). The δv_{rms} of Case 11 with only the relatively cold structures are only slightly smaller than that of Case 1 (Figure 8b), suggesting that the temperature anomaly power is dominated by the slabs instead of plumes.

Cases 12 and 13 with longer model time (i.e., 200 and 458 Ma) display similar characteristics to Case 11, although they show more plumes than Case 11 (Figures 5p–5x). The plumes significantly reduce the correlations with seismic model mainly in the upper mantle for Case 12 (Figures 3, 10d, and 10e) and at ~700–1,500-km depths for Case 13 (Figures 3, 10g, and 10h), but the slab structures and their correlations with the seismically fast anomalies remain nearly the same as in Case 11 and other models (Figure 4). Also, both Cases 12 and 13 show noticeably smaller correlations with the seismic model near the CMB than Case 11 (Figures 10a, 10b, 10d, 10e, and 10g, and 10h). This is because the overall distribution of the plumes in Cases 12 and 13 differ more from that of the LLSVPs in seismic models (Figures 5u and 5x). The overall RMS power δv_{rms} for Cases 11–13 are similar at all the depths (Figure 8b), and compared with Case 1, the main difference is below 2,400-km depth near the bottom thermal boundary layer. Still, δv_{rms} of Cases 12 and 13 with only the relatively cold structures are similar to that of Case 11.

3.4. Effects of Different Viscosity Structures
3.4.1. Effects of Average Viscosity or Rayleigh Number
The absolute value of mantle viscosity determines effective Rayleigh number Ra and could affect mantle flow velocity and mantle convective structures. To examine such effects, we compute two isochemical, purely thermal convection models with 200-Ma plate motion history with different Ra. Cases 14 and 15 are identical to Case 12 except that Ra are 2×10^7 and 1×10^8, respectively (Ra is 5×10^7 in Case 12 as in all the other cases presented so far in Table 2). With a smaller Ra at 2×10^7, the plumes and slabs in Case 14 are thicker than those in Case 12 (Figures 5s–5u and 11a–11c), while with a larger Ra, Case 15 shows thinner and more plumes and slabs (Figures 11d–11f). Therefore, the RMS power δv_{rms} is generally smaller for larger Ra and the vice versa (Figure 8c). Both Cases 14 and 15 have much worse correlations with SEMUCB-WM1 than Case 12 with Ra = 5×10^7, not only for the full structures but also for the slab structures (Figures 3 and 4). Notice that Ra = 5×10^7 is the preferred, because it leads to averaged lower mantle viscosity of ~2.5×10^{22} Pa·s that is consistent with postglacial rebound studies as discussed in the model setup section, and also because with this Ra, Case 12 has better correlations with seismic models. Although 200 Myr appears to be sufficient for plume and slab structures to fully develop with Ra = 5×10^7 or higher (Figure 8b), it seems too short for Ra = 2×10^7 in Case 14 to fully develop structures in the lowermost lower mantle. Therefore, we computed Case 16 that includes 458-Myr plate motion history (e.g., Zhang et al., 2010) but is otherwise identical to Case 14. However, this does not improve the correlations to the seismic model,
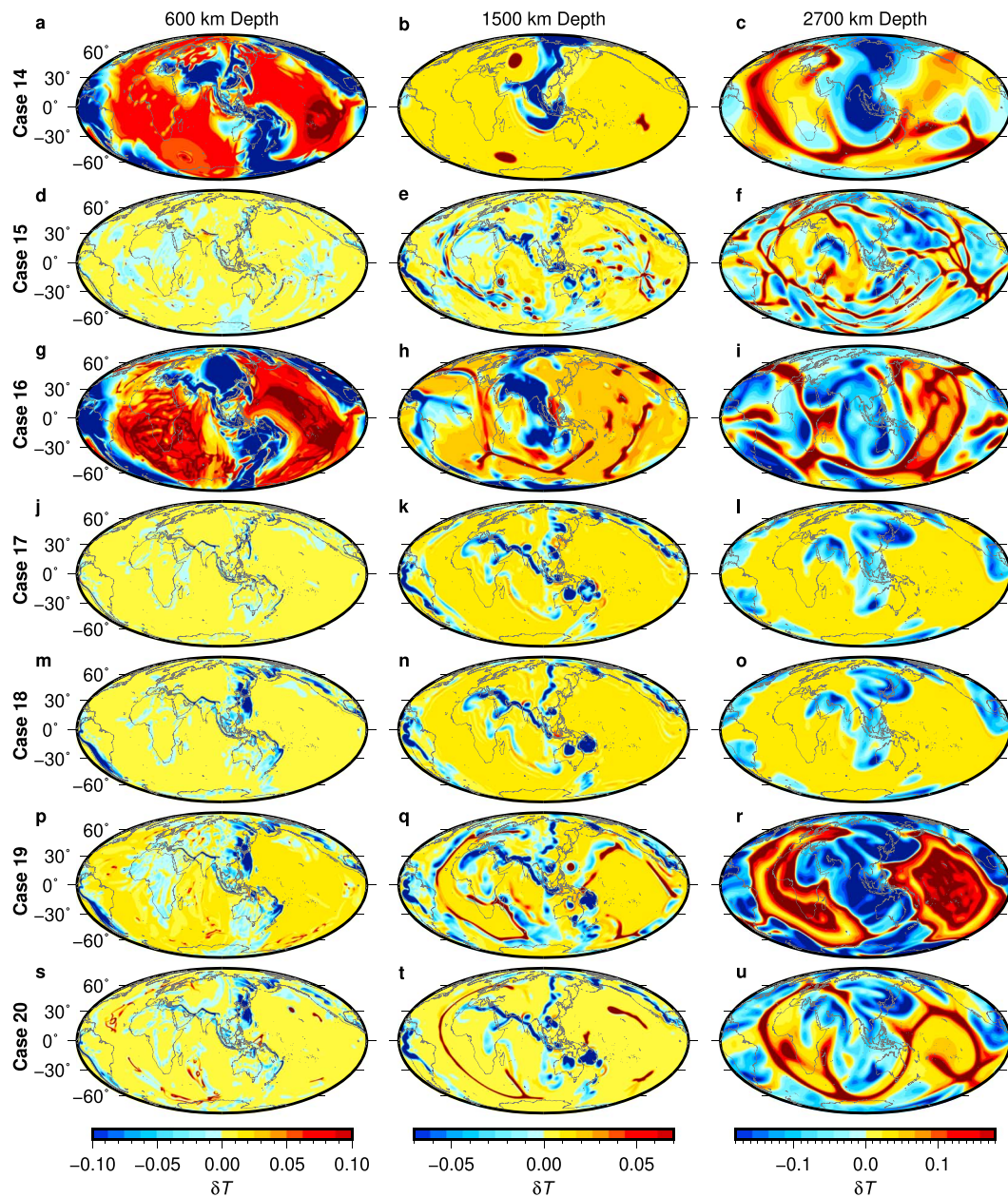
Figure 11. Same as Figure 5 but for Cases 14–20 that focus on the effects of different viscosity structures.

compared with Case 14 (Figures 3 and 4). The RMS power δv_{rms} of Case 16 is significantly larger than that of Case 14 (Figure 8c), as more structures are developed in Case 16.

3.4.2. Effects of the 1,000-km Depth Viscosity Discontinuity

To account for proposed seismic structural change at ~1,000-km depth (e.g., French & Romanowicz, 2015), Rudolph et al. (2015) suggested a viscosity increase at that depth. In order to evaluate the effects of a viscosity increase at the 1,000-km depth on mantle convective structures and their comparison with seismic tomographic models, we have computed four additional cases (Cases 17–20 in Table 2). We first present Case 17 that is identical to Case 2 except that the viscosity jump is at 1,000-km depth instead of 670-km depth (i.e., no phase change). Cases 17 and 2 have similar slab structures throughout the mantle except at depths above 1,000 km (Figures 5d–5f and 11j–11l). More slabs appear at 1,000-km depth in Case 17 than Case 2 (Figures 12e and 12h), especially in the western Pacific, while less slabs are generated at 600-km depth in
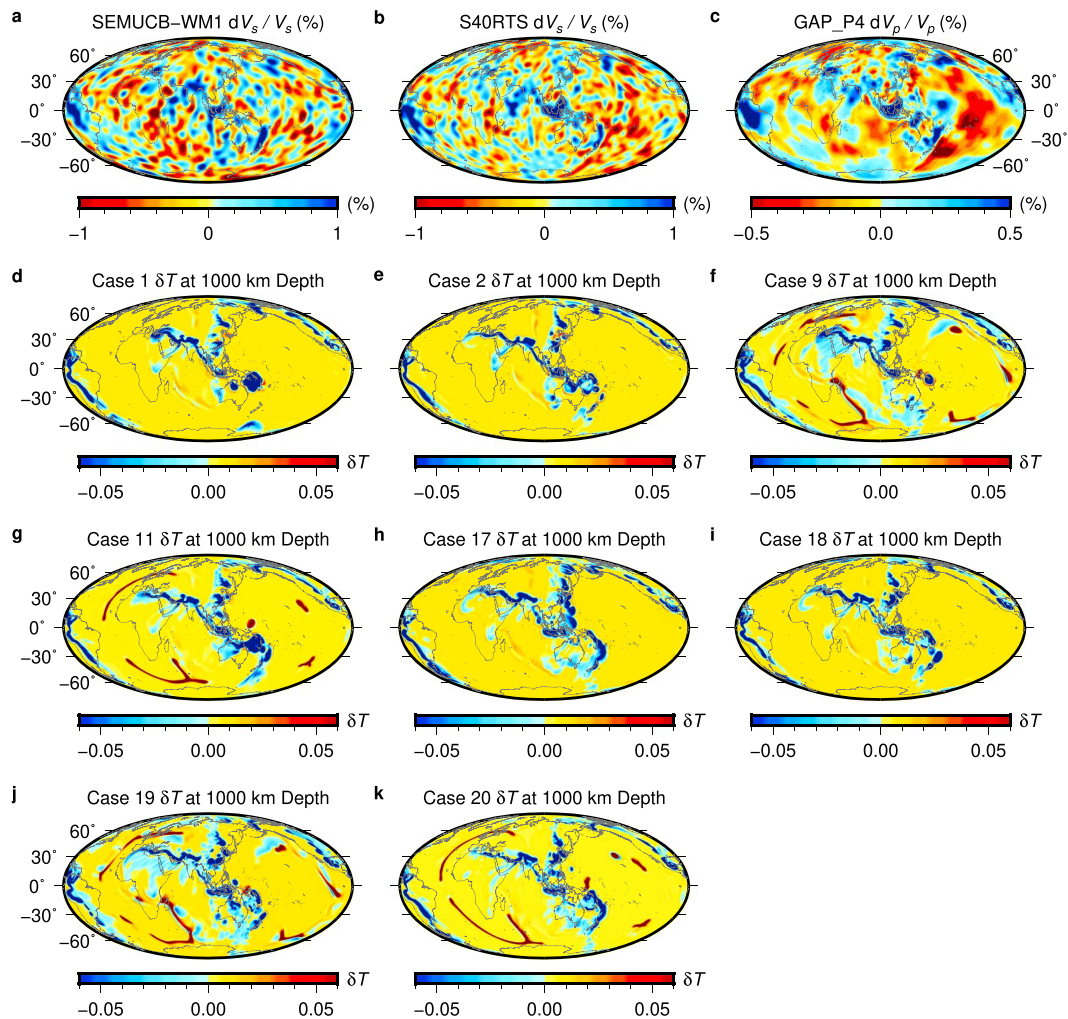
Figure 12. (a–c) Seismic velocity anomalies at 1,000-km depth for seismic models SEMUCB-WM1, S40RTS, and GAP_P4. (d–k) Present-day dimensionless temperature anomalies at 1,000-km depth for convection models Cases 1, 2, 9, 11, and 17–20, respectively.

Case 17 than Case 2 (Figures 5d and 11j). The correlations of Case 17 with SEMUCB-WM1 are generally consistent with but slightly worse than those of Case 2 (Figures 3, 4, 6d, 6e, and 13a, and 13b). However, as pointed out earlier, the agreement between seismic tomographic models appears to be the worst at ~1,000-km depth (Figures 2a, 2b, and 12a–12c). It should also be pointed out that neither of Cases 17 and 2 reproduces stagnant structures in the mantle transition zone which are more robust seismic structures. The RMS power of mantle structure has a minor increase at ~1,000-km depth in Case 17, while the power increase occurs at ~700-km depth in Case 2 (Figures 6f and 13c), showing the effect of viscosity increase. The RMS powers are otherwise quite similar between these two cases.

Case 18 is identical to Case 17 except for including the phase transition with Clapeyron slope of −2.0 MPa/K at 670-km depth. Compared with Case 1, Case 18 does not have the weak layer beneath 670-km depth and the viscosity jump is at 1,000-km depth instead of 670-km depth. Interestingly, Case 18 shows similar slab structures to Case 1 throughout the mantle including the stagnant slabs in the mantle transition zone (Figures 11m–11o), and Case 18 produces even slightly better correlations with SEMUCB-WM1 than Case 1 at intermediate- and short-wavelength bands (degrees 4–20; Figures 3 and 4). At the 600-km depth and in the mantle transition zone, Case 18 shows similar stagnant slab structures to Case 1, especially in the Northern Honshu (Figures 11m and S8l–S8o). Case 18 correlates with the seismic model much better than Case 17 (Figures 3 and 4), showing the important effect of the 670-km depth phase change. Apart from the localized peak of the RMS power δv_{rms} at ~670-km depth due to the phase transition, Case 18 also has
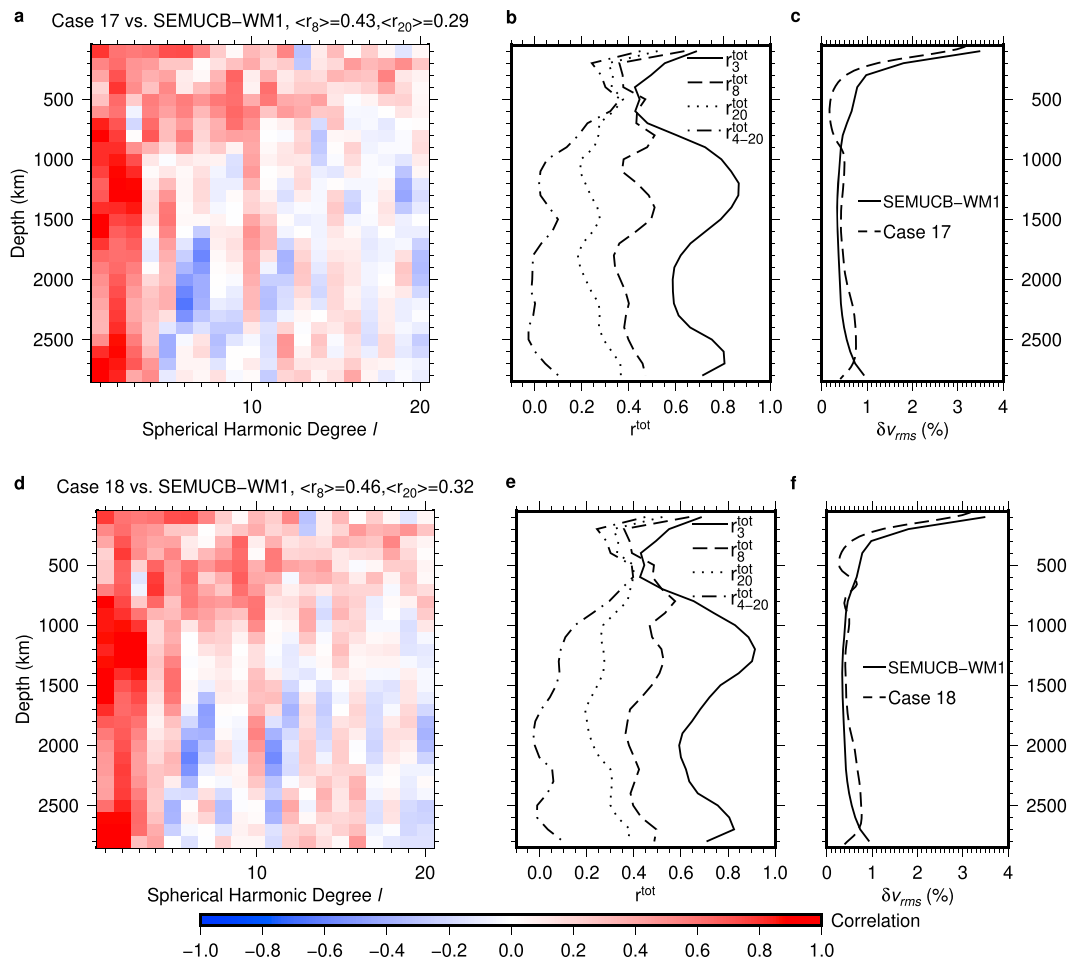
Figure 13. Same as Figure 6 but for Cases (a–c) 17 and (d–f) 18.

another localized peak at ~1,000-km depth due to the increase of viscosity (Figure 13f). That Case 18 reproduces the stagnant slabs in the mantle transition zone similar to Case 1 can be understood in terms of the same lubricating process from the weak layer in Case 1 (MZ18). In Case 18, with the 100 times of viscosity increase at 1,000-km depth, the mantle below the 670-km phase change is similarly weak as in Case 1, leading to reduced viscous resistance to horizontal spreading of slabs above the phase change (MZ18).

In order to evaluate potential effects of the viscosity jump at 1,000-km depth on plumes and LLSVPs, we also compute Cases 19 and 20 that employ an isothermal CMB condition that permits generation of mantle plumes. Cases 19 and 20 are modified from Cases 9 and 11 which correlate the best with SEMUCB-WM1 in the lowermost lower mantle, as discussed in section 3.3. Case 19 with chemically dense layer near the CMB is identical to Case 9, except that Case 19 excludes the weak layer and the 100 times viscosity increase is at 1,000 km instead of 670-km depth. Case 20 differs from Case 19 in excluding the chemically dense layer and the different total model time. Both the slab and LLSVP-like structures in Cases 9 and 11 are preserved in Cases 19 and 20 with the new viscosity (Figures 11p–11u). The total weighted correlations between Case 19 and SEMUCB-WM1 ($<r_3> = 0.70$, $<r_8> = 0.49$, and $<r_{20}> = 0.33$) are slightly reduced compared with Case 9 ($<r_3> = 0.71$, $<r_8> = 0.50$, and $<r_{20}> = 0.34$), and similar conclusion can be made for Case 20 relative to Case 11 (Figures S13a, S13b, S13d, S13e, 7d, 7e, 10a, and 10b). Therefore, to move the viscosity jump from 670- to 1,000-km depth does not change correlations of convection models with SEMUCB-WM1 when plumes and thermochemical piles are taken into account.

3.5. The Effect of Different Plate Motion History

The plate motion history (e.g., Seton et al., 2012) used in our models may have different uncertainties at different times and could affect the overall convection structures. We also test another plate motion history by Müller et al. (2016). Cases 21 and 22 are identical to Cases 1 and 7, respectively, except using the new plate motion model. The overall correlations between Case 21 and SEMUCB-WM1 are nearly identical to those between Case 1 and SEMUCB-WM1 at all wavelength bands. The same conclusion can be made for Cases 22 and 7 (Figures 3 and 4). Therefore, we suggest that our overall results are not sensitive to the difference between plate motion history models in Seton et al. (2012) and Müller et al. (2016).

4. Discussions

As global seismic tomography models continuously improve, a number of robust features have emerged: the predominance of degree-2 structure throughout the mantle, the African and Pacific LLSVPs, and seismically fast anomalies of slabs including the stagnant slabs in the mantle transition zone and slabs in the lower mantle (e.g., French & Romanowicz, 2015; Fukao & Obayashi, 2013; Grand et al., 1997; Houser et al., 2008; Masters et al., 2000; Ritsema et al., 2011). Significant advance has also been made in global mantle convection modeling to explain these seismic structures from the lower mantle slabs (Bunge & Grand, 2000; Bunge et al., 1998; Ricard et al., 1993; Lithgow-Bertelloni & Richards, 1998; MZ18), to the LLSVPs above the CMB (Bower et al., 2013; McNamara & Zhong, 2005; Zhong & Rudolph, 2015), and to the stagnant slabs in the transition zone (MZ18). Our study systematically quantifies how well the global mantle convection models may reproduce the seismic structures and examines the effects of boundary conditions, plate motion history, chemical buoyancy, and viscosity (i.e., Rayleigh number) and its different layering (e.g., viscosity increase at 670- and 1,000-km depths).

4.1. How Well Mantle Convection Models Reproduce Seismic Structures?

In general, our convection models (e.g., Cases 1 and 9) reproduce well the main features in seismic tomographic models including stagnant slabs in the mantle transition zone in the western Pacific, deep slabs in the lower mantle of North America, Asia, and Tethys, and the African and Pacific LLSVPs in the lowermost lower mantle. Quantitative comparison between our convection models and seismic models in a spherical harmonic domain demonstrates that in the upper mantle and the uppermost lower mantle (<1,000-km depth), our convection models correlate well with seismic models at long to short wavelengths (e.g., $l =$ 1–3, 1–8, 1–20, and 4–20; Figures 3, 4, 6a, 6b, 7d, and 7e). However, in the deeper part of the lower mantle (>1,000-km depth), our convection models have significantly good correlations with seismic models only at relatively long wavelengths (i.e., from $l = 1$ to 3, or >13,000-km wavelengths) and moderately good correlations at relatively shorter wavelengths (i.e., $l = 4$–5, or 10,000–8,000-km wavelengths), but the correlations at even shorter wavelengths (i.e., $l > 5$, or <8,000-km wavelengths) are highly variable from positive to negative. Since correlations among seismic models at large depths (>1,000 km) are generally high for $l < 16$ (or >2,500-km wavelengths; Figure 2a), this suggests that our convection models are still significantly challenged and limited in modeling the lower mantle structure consistently. The challenges and limitations may be primarily due to the larger uncertainties in plate motion history for the more distant past and/or the lower mantle viscosity structure.

Our new slab-only mantle convection models (i.e., using an insulating CMB condition) by solving the conservation equations have better correlations with seismic tomographic models compared with previous slab-only models lrr98d (Lithgow-Bertelloni & Richards, 1998; Ricard et al., 1993) and stb00d (Steinberger, 2000) at different wavelength bands (e.g., $l =$ 1–3, 1–8, 1–20, and 4–20; Figures 3a and 4a). Especially in the mantle transition zone (Figures 3b and 4b), our convection models reproduce the stagnant slab structures that those previous slab models did not consider. And at 600-km depth r^{tot}_{20} with SEMUCB-WM1 in our slab-only models Cases 1 (130 Myr; Figure 6b) and 7 (200 Myr; Figure S10e) are 0.37 and 0.43, respectively, which are much better than models stb00d with $r^{tot}_{20} = 0.26$ and lrr98d with $r^{tot}_{20} = 0.24$. Several improvements in our convection models result in the better correlations with seismic models. First, we use the new and better constrained plate motion history models by Seton et al. (2012) and Müller et al. (2016). Second, lrr98d used empirical rules for slab advection without solving the convection governing equations, but our mantle convection models solve these equations. Third, stb00d

and the updated models in Steinberger et al. (2012) did not consider temperature-dependent viscosity, which may have significant effects on cold slab structures. Fourth, our models include the spinel-to-postspinel phase transition and a weak layer beneath the phase change that successfully reproduce the stagnant slab structures observed in seismic models.

Taking the plume or thermochemical pile structures into account, the correlations between our convection models and seismic tomographic models improve significantly in the lowermost lower mantle. Our best fit model is Case 9 with 200-Myr plate motion history in a thermochemical convection model, and its total weighted correlations with SEMUCB-WM1 are $<r_8> = 0.50$ and $<r_{20}> = 0.34$. At 2,700-km depth, the total correlations r^{tot}_3 and r^{tot}_8 are 0.91 and 0.66, respectively. Our best fit purely thermal convection model in the lowermost lower mantle, Case 11, also has similar correlations with SEMUCB-WM1 at 2,800-km depth, and r^{tot}_3 and r^{tot}_8 are 0.93 and 0.62, respectively.

Changing the reference seismic model does not affect our conclusions. If we take SMEAN (Becker & Boschi, 2002) as the reference model as previous studies did (Becker & Boschi, 2002; Steinberger et al., 2012), our slab-only models also have significantly larger correlations with SMEAN than previous models (Figure S14). stb00d has $<r_8> = 0.30$ and $<r_{20}> = 0.21$, lrr98d has $<r_8> = 0.33$ and $<r_{20}> = 0.18$, and the best fit slab-only model in Steinberger et al. (2012) has $<r_8> = 0.42$ and $<r_{20}> = 0.34$. However, Case 1 (130-Ma plate motion) has $<r_8> = 0.48$ and $<r_{20}> = 0.36$, and Case 7 (200-Ma plate motion) has $<r_8> = 0.52$, and $<r_{20}> = 0.38$. Taking the plumes and thermochemical piles into account, the model in Steinberger et al. (2012) has $<r_8> = 0.53$, and $<r_{20}> = 0.37$, while our thermochemical convection model Case 9 has $<r_8> = 0.53$, and $<r_{20}> = 0.39$. If S20RTS is taken as the reference model, the total correlation r^{tot}_{20} of our models are also significantly higher those in Shephard et al. (2012) whose models ignored the temperature-dependent viscosity and the phase change but considered plate motion models under different absolute reference frames. For example, at 600–1,500-km depths, r^{tot}_{20} of Case 1 is uniformly larger than 0.17 and is 0.44 at 600-km depth (Figures S15a and S15b), but in Shephard et al. (2012) r^{tot}_{20} is only half of those of Case 1 (see Shephard et al., 2012, Figure 7).

The RMS power distribution of our convection models are generally consistent with S wave velocity anomaly power distribution. Although we mostly present comparisons between our convection models with SEMUCB-WM1, our general results are the same when other seismic tomographic models considered in this study are taken as reference (Figures S3 and S16). If converted into density anomalies, they generally have similar amplitude. Except above the CMB, the amplitude in mantle convection model is larger than that in seismic model, which can be explained by irregular sampling and limited resolution in seismic models (Schuberth et al., 2009). It should be noted that the conversion factor we use in this study is constant throughout the mantle, while this factor may vary with depth (Karato & Karki, 2001; Simmons et al., 2009; Simmons et al., 2010).

4.2. Robustness of the Slab and LLSVP Structures

While the locations of slabs are dictated by the plate motion history, the locations of plumes that are formed from the CMB as a result of boundary layer instabilities are often not predictable (e.g., Li & Zhong, 2017). Additionally, as plumes ascend through the mantle, their trajectories would be affected by global mantle flow (e.g., Steinberger & O'Connell, 1998), as well as mantle rheology (Zhong et al., 2000). We found that the plume structures tend to reduce correlations significantly with seismic models in both purely thermal convection models (e.g., Figure 10 for Cases 11–13) and long-time run thermochemical models (e.g., Figures 7g and 7h for Case 10). However, in short-time run thermochemical convection models, the plume structures do not affect the correlations with seismic models in the upper mantle (e.g., Figures 7d and 7e for Case 9), because the plumes originated from thermochemical piles tend to be weaker with smaller temperature anomalies than the plumes originated from the CMB in purely thermal convection models (Li & Zhong, 2017; Tan et al., 2011).

The slab structures do not seem to be affected by the presence of plumes in both purely thermal and thermochemical convection models (Figures 5a–5c and 5j–5x) because plumes mostly occur far away from slab regions (e.g., Li & Zhong, 2017). This is supported by our calculations that show nearly the same correlations between the cold slab structures in our convection models and fast anomalies in seismic models (Figure 4), although the plumes may significantly reduce the correlations (Figure 3). This

suggests that both the fast velocity anomalies in seismic models and slab structures that are derived from plate motion history are robust features. Therefore, the use of the thermally insulating CMB boundary condition is suitable for studying slab structures in the relatively short geological time periods (65–200 Myr).

The weak layer beneath the mantle transition zone does not appear to affect other mantle structures (e.g., LLSVP), although it helps produce stagnant slabs in the mantle transition zone (Figures 5g–5x). The slab stagnation is only a temporary phenomenon that may last for 20–30 Myr and would not affect the long-time evolution of slab penetration into the lower mantle (MZ18). Therefore, the shapes of the thermochemical plies and plumes in the lowermost lower mantle, which are mainly affected by the subducted slabs above the CMB, are not affected.

Our purely thermal convection and thermochemical convection model calculations show that correlations with seismic tomographic models in the lowermost lower mantle alone cannot distinguish thermal and thermochemical origins of the LLSVP structures. This is consistent with previous studies (Bull et al., 2009; Lassak et al., 2010; Schuberth et al., 2009). Bull et al. (2009) applied the tomographic filter to convection models by considering the resolution of seismic model S20RTS and found that thermochemical or purely thermal models show equally good spectral characteristics as S20RTS in the lower mantle. Schuberth et al. (2009) also applied the tomographic filter and demonstrated that purely thermal model could reconcile the amplitude of S wave anomalies in the lower mantle. The joint inversion of seismic and geodynamic data by Simmons et al. (2009) suggests that purely thermal model could explain the observed S wave travel times, but the low correlation of S wave and P wave in the deep mantle requires some compositional contribution (Simmons et al., 2010). Instead, Davies et al. (2012) found that purely thermal mantle convection models with 300-Myr imposed surface plate motion could explain the S wave anomalies and gradients, and the presence of postperovskite could reconcile the high S wave to P wave anomaly ratios and anticorrelation between shear- and bulk-sound velocity anomalies.

4.3. The 1,000-km Viscosity Discontinuity

Fukao and Obayashi (2013) suggested that some of the slabs appear stalled at ~1,000-km depth based on their seismic model GAP_P4. French and Romanowicz (2015) proposed that the seismically slow anomalies (i.e., plumes) also have a structural change at ~1,000-km depth. A viscosity increase at 1,000-km depth was proposed based on geoid inversion studies and such a viscosity increase may offer an explanation of the seismic structure (Rudolph et al., 2015). However, seismic tomographic models do not seem to agree with the slab structures at ~1,000-km depth (MZ18; Goes et al., 2017). As pointed out in previous studies (French & Romanowicz, 2014; Meschede & Romanowicz, 2014), we also notice that SEMUCB-WM1 and S40RTS differ substantially at ~1,000-km depth at $l = 1$, so do other seismic models at this depth (Figures 2a, 2b, and S17). Our convection models show better correlation with SEMUCB-WM1 at $l = 1$ at ~1,000-km depth than with other seismic models included in this study (Figures 6a, S16a, S16d, and S16g). In addition, the geoid inversion for mantle viscosity is nonunique (e.g., King, 1995) and viscosity increase at 670-km depth could also successfully explain observed geoid (e.g., Hager & Richards, 1989; Liu & Zhong, 2016). The advantage of Rudolph et al. (2015) is its avoidance of a priori assumptions on viscosity variations with depth, but viscosity increase at 670-km depth may fit the geoid better than that at 1,000-km depth (Yang & Gurnis, 2016). Therefore, the dynamics of the mantle around ~1,000-km depth is still a highly debatable topic that requires more observational and geodynamic studies.

However, it is interesting to note that our slab-only convection model (Case 18) with the 670-km phase change and viscosity increase at 1,000-km depth produces extremely similar slab structures throughout the mantle to Case 1 with the 670-km phase change, a thin weak layer below the phase boundary, including the stagnant slab structures in the mantle transition zone and slabs in the lower mantle (Figures S2e–S2h and S8l–S8o). However, a viscosity increase at 1,000-km depth by itself without the phase change (Case 17) fails to produce the stagnant slabs in the mantle transition zone nor at ~1,000-km depth, suggesting an important role of the 670-km phase change. A significant difference between Cases 1 and 18 is with the northern Mariana slabs: although the slabs are deflected horizontally in the transition zone in both models, in Case 18 some segments of the slabs also descend into the lower mantle to ~1,000-km depth. Therefore, future high-resolution regional seismic tomographic models may help distinguish these two viscosity models. It should be noted that in Case 18, viscosity is increased by a factor of

100 at 1,000-km depth, while Rudolph et al. (2015) proposed a factor of ~20–30 viscosity increase. Finally, we suggest that Cases 1 and 18 produce horizontally deflected slabs in the mantle transition zone for the same reason; that is, the viscosity below the 670 km phase boundary is relatively small, being the thin weak layer in Case 1 or the uniformly weak layer above the 1,000-km depth in Case 18, which allows the slabs to spread horizontally.

Admittedly, our layered viscosity models with viscosity jumps at 670- and 1,000-km depths as in many previous studies are simplified, and viscosity variations may not necessarily occur at these depths or as a step function. Furthermore, there is a trade-off between the thickness and the viscosity of weak layer (either the asthenosphere or the weak layer beneath the mantle transition zone as we proposed here; e.g., Richards & Lenardic, 2018), such that the thinner the layer (e.g., the asthenosphere) is, the lower viscosity is required to achieve the same dynamic effect. However, most observations unfortunately do not have adequate depth resolution to place constraints on finer scale viscosity structures (e.g., Mitrovica, 1996; Paulson et al., 2007). Consequently, we have employed our simplified layer viscosity models.

5. Conclusions

In this study, we have computed 22 global mantle convection models with different mantle viscosity structure, CMB condition, plate motion history, and compositional structure. We compare different seismic tomographic models to identify robust and uncertain features. We compute correlations of convection models with seismic models to determine how well current generation of convection models may reproduce seismic structures, that is, the success and limitations of convection models. Our main conclusions are as follows:

1. Our convection models with a weak layer beneath the spinel-to-postspinel phase transition reproduce robust seismic structures in the mantle including stagnant slabs in the mantle transition zone in the western Pacific, deep slabs in the lower mantle of North America, Asia, and Tethys, and the African and Pacific LLSVPs in the lowermost lower mantle. The overall correlations between our convection and seismic models are high at long to short wavelengths (for spherical harmonic degree l from 1 to 20) in the upper mantle and mantle transition zone, but our convection models can only consistently reproduce relatively long-wavelength seismic structures (l from 1 to 3) below 1,000-km depth in the lower mantle.
2. Mantle plumes in global convection models may reduce the correlations with the seismic models in the upper mantle, but the plumes and thermochemical piles help improve the correlations in the lowermost lower mantle. However, the cold slab structures and their correlations with the seismically fast anomalies are nearly identical for our convection models with and without the plumes. This suggests that the plumes have a minor effect on slab structures in convection models and that the seismically fast anomalies mainly result from the subducted slabs.
3. When the 670-km phase change is included, our convection models with a viscosity increase at 1,000-km depth have similar correlations with seismic models compared with convection models with a thin weak layer below the 670-km phase boundary. Specifically, both models reproduce the stagnant slab structures in the mantle transition zone.
4. The correlations among different seismic models are high throughout the mantle except for at ~1,000-km depth, suggesting that more seismic studies are needed to resolve these differences at ~1,000-km depth.
5. Our convection modeling studies show that 130 Myr of plate motion history is sufficiently long to reproduce most of the seismically fast anomalies throughout the mantle in the seismic models (e.g., Bunge et al., 1998), but 65 Myr of plate motion history could only reproduce structures in the top 1,500 km of the mantle.
6. When the isothermal CMB condition is applied to cause mantle plume and LLSVP structures to form, purely thermal and thermochemical convection models have similarly good correlations with seismic models in the lowermost lower mantle and have better correlations with seismic models than slab-only (i.e., with insulating CMB condition) convection models. The thin weak layer beneath the mantle transition zone and the 670-km phase transition have minor effect on the LLSVP structures.
7. The temperature anomaly power is mainly controlled by slabs in most part of the mantle except in the lowermost lower mantle where plumes or thermochemical piles contribute significantly to the power.

References

Agrusta, R., Goes, S., & van Hunen, J. (2017). Subducting-slab transition-zone interaction: Stagnation, penetration and mode switches. *Earth and Planetary Science Letters*, *464*, 10–23. https://doi.org/10.1016/j.epsl.2017.02.005

Becker, T. W., & Boschi, L. (2002). A comparison of tomographic and geodynamic mantle models. *Geochemistry, Geophysics, Geosystems*, *3*(1), 1003. https://doi.org/10.1029/2001GC000168

Billen, M. I., & Hirth, G. (2007). Rheologic controls on slab dynamics. *Geochemistry, Geophysics, Geosystems*, *8*, Q08012. https://doi.org/10.1029/2007GC001597

Bower, D. J., Gurnis, M., & Seton, M. (2013). Lower mantle structure from paleogeographically constrained dynamic Earth models. *Geochemistry, Geophysics, Geosystems*, *14*, 44–63. https://doi.org/10.1029/2012GC004267

Bull, A. L., McNamara, A. K., & Ritsema, J. (2009). Synthetic tomography of plume clusters and thermochemical piles. *Earth and Planetary Science Letters*, *278*(3-4), 152–162. https://doi.org/10.1016/j.epsl.2008.11.018

Bunge, H. P., & Grand, S. P. (2000). Mesozoic plate-motion history below the Northeast Pacific Ocean from seismic images of the subducted Farallon slab. *Nature*, *405*(6784), 337–340. https://doi.org/10.1038/35012586

Bunge, H. P., Richards, M. A., Lithgow-Bertelloni, C., Baumgardner, J. R., Grand, S. P., & Romanowicz, B. A. (1998). Time scales and heterogeneous structure in geodynamic Earth models. *Science*, *280*(5360), 91–95. https://doi.org/10.1126/science.280.5360.91

Christensen, U. R. (1996). The influence of trench migration on slab penetration into the lower mantle. *Earth and Planetary Science Letters*, *140*(1-4), 27–39. https://doi.org/10.1016/0012-821X(96)00023-4

Christensen, U. R., & Yuen, D. A. (1985). Layered convection induced by phase transitions. *Journal of Geophysical Research*, *90*(B12), 10,291–10,300. https://doi.org/10.1029/JB090iB12p10291

Davaille, A. (1999). Simultaneous generation of hotspots and superswells by convection in a heterogeneous planetary mantle. *Nature*, *402*(6763), 756–760. https://doi.org/10.1038/45461

Davies, D. R., Goes, S., Davies, J. H., Schuberth, B. S. A., Bunge, H. P., & Ritsema, J. (2012). Reconciling dynamic and seismic models of Earth's lower mantle: The dominant role of thermal heterogeneity. *Earth and Planetary Science Letters*, *353-354*, 253–269. https://doi.org/10.1016/j.epsl.2012.08.016

Deschamps, F., Snieder, R., & Trampert, J. (2001). The relative density-to-shear velocity scaling in the uppermost mantle. *Physics of the Earth and Planetary Interiors*, *124*(3-4), 193–212. https://doi.org/10.1016/S0031-9201(01)00199-6

Dziewonski, A. M., Hager, B. H., & O'Connell, R. J. (1977). Large-scale heterogeneities in the lower mantle. *Journal of Geophysical Research*, *82*(2), 239–255. https://doi.org/10.1029/JB082i002p00239

Eckhardt, D. H. (1984). Correlations between global features of terrestrial fields. *Mathematical Geology*, *16*(2), 155–171. https://doi.org/10.1007/BF01032214

French, S. W., & Romanowicz, B. (2015). Broad plumes rooted at the base of the Earth's mantle beneath major hotspots. *Nature*, *525*(7567), 95–99. https://doi.org/10.1038/nature14876

French, S. W., & Romanowicz, B. A. (2014). Whole-mantle radially anisotropic shear velocity structure from spectral-element waveform tomography. *Geophysical Journal International*, *199*(3), 1303–1327. https://doi.org/10.1093/gji/ggu334

Fukao, Y., & Obayashi, M. (2013). Subducted slabs stagnant above, penetrating through, and trapped below the 660 km discontinuity. *Journal of Geophysical Research: Solid Earth*, *118*, 5920–5938. https://doi.org/10.1002/2013JB010466

Fukao, Y., Obayashi, M., Nakakuki, T., & Deep Slab Project Group (2009). Stagnant slab: A review. *Annual Review of Earth and Planetary Sciences*, *37*(1), 19–46. https://doi.org/10.1146/annurev.earth.36.031207.124224

Fukao, Y., Widiyantoro, S., & Obayashi, M. (2001). Stagnant slabs in the upper and lower mantle transition region. *Reviews of Geophysics*, *39*(3), 291–323. https://doi.org/10.1029/1999RG000068

Garel, F., Goes, S., Davies, D. R., Davies, J. H., Kramer, S. C., & Wilson, C. R. (2014). Interaction of subducted slabs with the mantle transition-zone: A regime diagram from 2-D thermomechanical models with a mobile trench and an overriding plate. *Geochemistry, Geophysics, Geosystems*, *15*, 1739–1765. https://doi.org/10.1002/2014GC005257

Garnero, E. J., McNamara, A. K., & Shim, S. H. (2016). Continent-sized anomalous zones with low seismic velocity at the base of Earth's mantle. *Nature Geoscience*, *9*(7), 481–489. https://doi.org/10.1038/ngeo2733

Goes, S., Agrusta, R., Van Hunen, J., & Garel, F. (2017). Subduction-transition zone interaction: A review. *Geosphere*, *13*(3), 644–664. https://doi.org/10.1130/GES01476.1

Grand, S. P., van der Hilst, R. D., & Widiyantoro, S. (1997). High resolution global tomography: A snapshot of convection in the Earth. *GSA Today*, *7*(4), 1–7.

Hager, B. H., Clayton, R. W., Richards, M. A., Comer, R. P., & Dziewonski, A. M. (1985). Lower mantle heterogeneity, dynamic topography and the geoid. *Nature*, *313*(6003), 541–545. https://doi.org/10.1038/313541a0

Hager, B. H., & Richards, M. A. (1989). Long-wavelength variations in Earth's geoid: Physical models and dynamical implications. *Philosophical Transactions of the Royal Society A*, *328*(1599), 309–327. https://doi.org/10.1098/rsta.1989.0038

He, Y., & Wen, L. (2012). Geographic boundary of the "Pacific Anomaly" and its geometry and transitional structure in the north. *Journal of Geophysical Research*, *117*, B09308. https://doi.org/10.1029/2012JB009436

Hofmann, A. W. (1997). Mantle geochemistry: The message from oceanic volcanism. *Nature*, *385*(6613), 219–229. https://doi.org/10.1038/385219a0

Holt, A. F., Becker, T. W., & Buffett, B. A. (2015). Trench migration and overriding plate stress in dynamic subduction models. *Geophysical Journal International*, *201*(1), 172–192. https://doi.org/10.1093/gji/ggv011

Houser, C., Masters, G., Shearer, P., & Laske, G. (2008). Shear and compressional velocity models of the mantle from cluster analysis of long-period waveforms. *Geophysical Journal International*, *174*(1), 195–212. https://doi.org/10.1111/j.1365-246X.2008.03763.x

van der Hilst, R. D., Widiyantoro, S., & Engdahl, E. R. (1997). Evidence for deep mantle circulation from global tomography. *Nature*, *386*(6625), 578–584. https://doi.org/10.1038/386578a0

Ishii, M., & Tromp, J. (1999). Normal-mode and free-air gravity constraints on lateral variations in velocity and density of Earth's mantle. *Science*, *285*(5431), 1231–1236. https://doi.org/10.1126/science.285.5431.1231

Jordan, T. H. (1975). The continental tectosphere. *Reviews of Geophysics and Space Physics*, *13*(3), 1–12. https://doi.org/10.1029/RG013i003p00001

Karato, S.-I. (1993). Importance of anelasticity in the interpretation of seismic tomography. *Geophysical Research Letters*, *20*(15), 1623–1626. https://doi.org/10.1029/93GL01767

Karato, S.-I. (2008). *Deformation of earth materials: An introduction to the rheology of solid earth*. New York: Cambridge University Press. https://doi.org/10.1017/CBO9780511804892

Karato, S.-I., & Karki, B. B. (2001). Origin of lateral variation of seismic wave velocities and density in the deep mantle. *Journal of Geophysical Research*, *106*(B10), 21,771–21,783. https://doi.org/10.1029/2001JB000214

King, S. D. (1995). Radial models of mantle viscosity: Results from a genetic algorithm. *Geophysical Journal International*, *122*(3), 725–734. https://doi.org/10.1111/j.1365-246X.1995.tb06831.x

Lassak, T. M., McNamara, A. K., Garnero, E. J., & Zhong, S. (2010). Core–mantle boundary topography as a possible constraint on lower mantle chemistry and dynamics. *Earth and Planetary Science Letters*, *289*(1-2), 232–241. https://doi.org/10.1016/j.epsl.2009.11.012

Lee, C., & King, S. D. (2011). Dynamic buckling of subducting slabs reconciles geological and geophysical observations. *Earth and Planetary Science Letters*, *312*(3-4), 360–370. https://doi.org/10.1016/j.epsl.2011.10.033

Leng, W., & Zhong, S. (2008). Controls on plume heat flux and plume excess temperature. *Journal of Geophysical Research*, *113*, B04408. https://doi.org/10.1029/2007JB005155

Li, M. M., Black, B., Zhong, S., Manga, M., Rudolph, M. L., & Olson, P. (2016). Quantifying melt production and degassing rate at mid-ocean ridges from global mantle convection models with plate motion history. *Geochemistry, Geophysics, Geosystems*, *17*, 2884–2904. https://doi.org/10.1002/2016GC006439

Li, M. M., & Zhong, S. (2017). The source location of mantle plumes from 3D spherical models of mantle convection. *Earth and Planetary Science Letters*, *478*, 47–57. https://doi.org/10.1016/j.epsl.2017.08.033

Lithgow-Bertelloni, C., & Richards, M. A. (1998). The dynamics of Cenozoic and Mesozoic plate motions. *Reviews of Geophysics*, *36*(1), 27–78. https://doi.org/10.1029/97RG02282

Liu, L., Spasojević, S., & Gurnis, M. (2008). Reconstructing Farallon plate subduction beneath North America back to the Late Cretaceous. *Science*, *322*(5903), 934–938. https://doi.org/10.1126/science.1162921

Liu, X., & Zhong, S. (2016). Constraining mantle viscosity structure for a thermochemical mantle using the geoid observation. *Geochemistry, Geophysics, Geosystems*, *17*, 895–913. https://doi.org/10.1002/2015GC006161

Mao, W., & Zhong, S. (2018). Slab stagnation due to a reduced viscosity layer beneath the mantle transition zone. *Nature Geoscience*, *11*(11), 876–881. https://doi.org/10.1038/s41561-018-0225-2

Masters, G., Laske, G., Bolton, H., & Dziewonski, A. (2000). The relative behavior of shear velocity, bulk sound speed, and compressional velocity in the mantle: Implications for chemical and thermal structure. In S. Karato (Ed.), *Earth's deep interior: Mineral physics and tomography*, AGU Monograph (Vol. 117, pp. 63–87). Washington, DC: American Geophysical Union.

McNamara, A. K., & Zhong, S. (2004). Thermochemical structures within a spherical mantle: Superplumes or piles? *Journal of Geophysical Research*, *109*, B07402. https://doi.org/10.1029/2003JB002847

McNamara, A. K., & Zhong, S. (2005). Thermochemical structures beneath Africa and the Pacific Ocean. *Nature*, *437*(7062), 1136–1139. https://doi.org/10.1038/nature04066

Meschede, M., & Romanowicz, B. (2014). Lateral heterogeneity scales in regional and global upper mantle shear velocity models. *Geophysical Journal International*, *200*(2), 1078–1095. https://doi.org/10.1093/gji/ggu424

Mitrovica, J. X. (1996). Haskell [1935] revisited. *Journal of Geophysical Research*, *101*(B1), 555–569. https://doi.org/10.1029/95JB03208

Mitrovica, J. X., & Forte, A. M. (2004). A new inference of mantle viscosity based upon joint inversion of convection and glacial isostatic adjustment data. *Earth and Planetary Science Letters*, *225*(1-2), 177–189. https://doi.org/10.1016/j.epsl.2004.06.005

Müller, R. D., Dutkiewicz, A., Seton, M., & Gaina, C. (2013). Seawater chemistry driven by supercontinent assembly, breakup, and dispersal. *Geology*, *41*(8), 907–910. https://doi.org/10.1130/G34405.1

Müller, R. D., Seton, M., Zahirovic, S., Williams, S. E., Matthews, K. J., Wright, N. M., et al. (2016). Ocean basin evolution and global-scale plate reorganization events since Pangea breakup. *Annual Review of Earth and Planetary Sciences*, *44*(1), 107–138. https://doi.org/10.1146/annurev-earth-060115-012211

Ni, S., Tan, E., Gurnis, M., & Helmberger, D. (2002). Sharp sides to the African superplume. *Science*, *296*(5574), 1850–1852. https://doi.org/10.1126/science.1070698

Panasyuk, S. V., & Hager, B. H. (1998). A model of transformational superplasticity in the upper mantle. *Geophysical Journal International*, *133*(3), 741–755. https://doi.org/10.1046/j.1365-246X.1998.00539.x

Panning, M., & Romanowicz, B. (2006). A three-dimensional radially anisotropic model of shear velocity in the whole mantle. *Geophysical Journal International*, *167*(1), 361–379. https://doi.org/10.1111/j.1365-246X.2006.03100.x

Paulson, A., Zhong, S., & Wahr, J. (2007). Limitations on the inversion for mantle viscosity from postglacial rebound. *Geophysical Journal International*, *168*(3), 1195–1209. https://doi.org/10.1111/j.1365-246X.2006.03222.x

Ricard, Y., Richards, M., Lithgow-Bertelloni, C., & Le Stunff, Y. (1993). A geodynamic model of mantle density heterogeneity. *Journal of Geophysical Research*, *98*(B12), 21,895–21,909. https://doi.org/10.1029/93JB02216

Richards, M. A., & Lenardic, A. (2018). The Cathles parameter (Ct): A geodynamic definition of the asthenosphere and implications for the nature of plate tectonics. *Geochemistry, Geophysics, Geosystems*, *19*, 4858–4875. https://doi.org/10.1029/2018GC007664

Ritsema, J., Deuss, A. A., Van Heijst, H. J., & Woodhouse, J. H. (2011). S40RTS: A degree-40 shear-velocity model for the mantle from new Rayleigh wave dispersion, teleseismic traveltime and normal-mode splitting function measurements. *Geophysical Journal International*, *184*(3), 1223–1236. https://doi.org/10.1111/j.1365-246X.2010.04884.x

Ritsema, J., van Heijst, H. J., & Woodhouse, J. H. (1999). Complex shear wave velocity structure imaged beneath Africa and Iceland. *Science*, *286*(5446), 1925–1928. https://doi.org/10.1126/science.286.5446.1925

Ritzwoller, M. H., Shapiro, N. M., & Zhong, S. J. (2004). Cooling history of the Pacific lithosphere. *Earth and Planetary Science Letters*, *226*(1-2), 69–84. https://doi.org/10.1016/j.epsl.2004.07.032

Rudolph, M. L., Lekić, V., & Lithgow-Bertelloni, C. (2015). Viscosity jump in Earth's mid-mantle. *Science*, *350*(6266), 1349–1352. https://doi.org/10.1126/science.aad1929

Schuberth, B. S. A., Bunge, H. P., & Ritsema, J. (2009). Tomographic filtering of high-resolution mantle circulation models: Can seismic heterogeneity be explained by temperature alone? *Geochemistry, Geophysics, Geosystems*, *10*, Q05W03. https://doi.org/10.1029/2009GC002401

Seton, M., Müller, R. D., Zahirovic, S., Gaina, C., Torsvik, T., Shephard, G., et al. (2012). Global continental and ocean basin reconstructions since 200 Ma. *Earth-Science Reviews*, *113*(3-4), 212–270. https://doi.org/10.1016/j.earscirev.2012.03.002

Shephard, G. E., Bunge, H. P., Schuberth, B. S., Müller, R. D., Talsma, A. S., Moder, C., & Landgrebe, T. C. W. (2012). Testing absolute plate reference frames and the implications for the generation of geodynamic mantle heterogeneity structure. *Earth and Planetary Science Letters*, *317-318*, 204–217. https://doi.org/10.1016/j.epsl.2011.11.027

Simmons, N. A., Forte, A. M., Boschi, L., & Grand, S. P. (2010). GyPSuM: A joint tomographic model of mantle density and seismic wave speeds. *Journal of Geophysical Research*, *115*, B12310. https://doi.org/10.1029/2010JB007631

Simmons, N. A., Forte, A. M., & Grand, S. P. (2009). Joint seismic, geodynamic and mineral physical constraints on three-dimensional mantle heterogeneity: Implications for the relative importance of thermal versus compositional heterogeneity. *Geophysical Journal International*, *177*(3), 1284–1304. https://doi.org/10.1111/j.1365-246X.2009.04133.x

Stegman, D. R., Freeman, J., Schellart, W. P., Moresi, L., & May, D. (2006). Influence of trench width on subduction hinge retreat rates in 3-D models of slab rollback. *Geochemistry, Geophysics, Geosystems*, *7*, Q03012. https://doi.org/10.1029/2005GC001056

Steinberger, B. (2000). Slabs in the lower mantle-results of dynamic modelling compared with tomographic images and the geoid. *Physics of the Earth and Planetary Interiors*, *118*(3-4), 241–257. https://doi.org/10.1016/S0031-9201(99)00172-7

Steinberger, B., & O'Connell, R. J. (1998). Advection of plumes in mantle flow: implications for hotspot motion, mantle viscosity and plume distribution. *Geophysical Journal International*, *132*(2), 412–434. https://doi.org/10.1046/j.1365-246x.1998.00447.x

Steinberger, B., Torsvik, T. H., & Becker, T. W. (2012). Subduction to the lower mantle—A comparison between geodynamic and tomographic models. *Solid Earth*, *3*(2), 415–432. https://doi.org/10.5194/se-3-415-2012

Su, W. J., & Dziewonski, A. M. (1997). Simultaneous inversion for 3-D variations in shear and bulk velocity in the mantle. *Physics of the Earth and Planetary Interiors*, *100*(1–4), 135–156. https://doi.org/10.1016/S0031-9201(96)03236-0

Su, W. J., Woodward, R. L., & Dziewonski, A. M. (1994). Degree 12 model of shear velocity heterogeneity in the mantle. *Journal of Geophysical Research*, *99*(B4), 6945–6980. https://doi.org/10.1029/93JB03408

Tan, E., Leng, W., Zhong, S., & Gurnis, M. (2011). On the location of plumes and lateral movement of thermochemical structures with high bulk modulus in the 3-D compressible mantle. *Geochemistry, Geophysics, Geosystems*, *12*, Q07005. https://doi.org/10.1029/2011GC003665

Tanimoto, T. (1990). Long-wavelength *S*-wave velocity structure throughout the mantle. *Geophysical Journal International*, *100*(3), 327–336. https://doi.org/10.1111/j.1365-246X.1990.tb00688.x

Turcotte, D. L., & Schubert, G. (2014). *Geodynamics* (3rd ed., pp. 192–193). Cambridge: Cambridge University Press.

Wen, L., Silver, P., James, D., & Kuehnel, R. (2001). Seismic evidence for a thermo-chemical boundary at the base of the Earth's mantle. *Earth and Planetary Science Letters*, *189*(3-4), 141–153. https://doi.org/10.1016/S0012-821X(01)00365-X

Yang, T., & Gurnis, M. (2016). Dynamic topography, gravity and the role of lateral viscosity variations from inversion of global mantle flow. *Geophysical Journal International*, *207*(2), 1186–1202. https://doi.org/10.1093/gji/ggw335

Yang, T., Moresi, L., Zhao, D., Sandiford, D., & Whittaker, J. (2018). Cenozoic lithospheric deformation in Northeast Asia and the rapidly-aging Pacific Plate. *Earth and Planetary Science Letters*, *492*, 1–11. https://doi.org/10.1016/j.epsl.2018.03.057

Zhang, N., Zhong, S., & Flowers, R. M. (2012). Predicting and testing continental vertical motion histories since the Paleozoic. *Earth and Planetary Science Letters*, *317-318*, 426–435. https://doi.org/10.1016/j.epsl.2011.10.041

Zhang, N., Zhong, S., Leng, W., & Li, Z. X. (2010). A model for the evolution of the Earth's mantle structure since the Early Paleozoic. *Journal of Geophysical Research*, *115*, B06401. https://doi.org/10.1029/2009JB006896

Zhong, S. (2006). Constraints on thermochemical convection of the mantle from plume heat flux, plume excess temperature, and upper mantle temperature. *Journal of Geophysical Research*, *111*, B04409. https://doi.org/10.1029/2005JB003972

Zhong, S., & Gurnis, M. (1994). Role of plates and temperature-dependent viscosity in phase change dynamics. *Journal of Geophysical Research*, *99*(B8), 15,903–15,917. https://doi.org/10.1029/94JB00545

Zhong, S., & Gurnis, M. (1995). Mantle convection with plates and mobile, faulted plate margins. *Science*, *267*(5199), 838–843. https://doi.org/10.1126/science.267.5199.838

Zhong, S., & Liu, X. (2016). The long-wavelength mantle structure and dynamics and implications for large-scale tectonics and volcanism in the Phanerozoic. *Gondwana Research*, *29*(1), 83–104. https://doi.org/10.1016/j.gr.2015.07.007

Zhong, S., McNamara, A., Tan, E., Moresi, L., & Gurnis, M. (2008). A benchmark study on mantle convection in a 3-D spherical shell using CitcomS. *Geochemistry, Geophysics, Geosystems*, *9*, Q10017. https://doi.org/10.1029/2008GC002048

Zhong, S., & Rudolph, M. L. (2015). On the temporal evolution of long-wavelength mantle structure of the Earth since the early Paleozoic. *Geochemistry, Geophysics, Geosystems*, *16*, 1599–1615. https://doi.org/10.1002/2015GC005782

Zhong, S., Zuber, M. T., Moresi, L., & Gurnis, M. (2000). Role of temperature-dependent viscosity and surface plates in spherical shell models of mantle convection. *Journal of Geophysical Research*, *105*(B5), 11,063–11,082. https://doi.org/10.1029/2000JB900003